Multiscalar 3D-temporal structural characterisation of Smøla Island, Mid-Norwegian passive margin: an analogue for unravelling the tectonic history of offshore basement highs

Matthew S. Hodge[1]*, Guri Venvik[2], Jochen Knies[2], Roelant van der Lelij[2], Jasmin Schönenberger[2], Øystein Nordgulen[2], Marco Brönner[2], Aziz Nasuti[2], & Giulio Viola[1]

1: Department of Biological, Geological and Environmental Sciences, University of Bologna, Italy

2: Geological Survey of Norway (NGU), Trondheim, Norway

Correspondence to: Matthew S. Hodge (matthew.hodge@unibo.it)

Abstract. Smøla Island, situated within the Mid-Norwegian passive margin, contains crystalline basement-hosted intricate fracture and fault arrays formed during a polyphase brittle tectonic evolution. Its detailed study may potentially strengthen correlative efforts between the well-exposed onshore domain and the inaccessible offshore domain and improve our understanding of the passive margin evolution. Integrating geophysical and remote sensing lineament analysis, along with field mapping, high resolution drill hole logging, three-dimensional (3D) modelling, petrographic and microstructural data, and fault gouge K-Ar geochronology, we identify five deformation episodes having affected Smøla through time: I) D_1 caused sinistral transtension leading to syn- to post-Devonian epidote-prehnite steep ENE-WSW tensile veins and sinistral shears related to the post-Caledonian evolution of the Møre Trøndelag Fault Complex (MTCF), and a later ~N-S contraction associated with inclined NW-SE normal, and ~NNW-SSE to NNE-SSW strike-slip features. II) D_2 formed diffuse sericite-chlorite-calcite structures during two phases in the Carboniferous (~300 Ma) and Late Triassic-Early Jurassic (~204-196 Ma). The first, associated with sinistral strike-slip movements along the MTFC, produced ~E-W and NE-SW sinistral strike-slip faults and fractures, ~N-S normal faults, and ENE-WSW reverse faults. The second, associated with MTFC dextral strike-slip faulting, formed ENE-WSW dextral strike-slip faults, ~N-S reverse faults, and ~E-W to NE-SW normal faults. III) D_3 formed chlorite-hematite breccias and gouges in response to Cretaceous (~128-100 Ma) extension, half-graben development and deepening of local basins. This episode is associated with normal to oblique-normal faults striking NNE-SSW and NE-SW. IV) D_4 is responsible for the formation of hematite-zeolite-calcite features, which formed after ~75 Ma during Cretaceous to Late Cretaceous crustal extension, associated with NNE-SSW, NE-SW normal dip-slip faults or tensile veins. V) D_5 formed NE-SW and NW-SE striking quartz-calcite shear and tensile veins during continued crustal extension preceding the Greenland-Norway break-up. Multiscalar modelling at scales of 100 m, 10 m, and 1 m shows the extent and size of deformation zones, with D_2 structures exhibiting the greatest strike continuity and D_1 features the most localised. Overall, the approach presented

here is of great utility for on/offshore correlation and studying basement volumes, particularly with complex brittle tectonic histories.

1 Introduction

Offshore crystalline basement highs are important structural elements of rifted passive margins (Peron-Pinvidic et al., 2013; Zastrozhnov et al., 2020). However, accessing and studying these features is challenging due to their locations beneath deep oceanic waters and younger sedimentary cover. Constraining their structural characteristics and tectonic evolution typically relies on relatively low-resolution datasets, such as seismic surveys and scattered drill hole data (e.g. Holdsworth et al., 2019; Tanner et al., 2020), which limits detailed reconstructions. Most of the geological knowledge on offshore basement highs derives from hydrocarbon exploration work, which, until recently mostly focussed on and around their faulted outermost edges, with limited interest in the basement volumes themselves (Riber et al., 2015). On the other hand, following indications that fractured and weathered basement may represent productive unconventional hydrocarbon reservoirs or act as pathways for oil and gas migration, they have recently begun to receive considerable attention (e.g. Hartz et al., 2013; Trice, 2014; Riber et al., 2015; Belaidi et al., 2018; Holdsworth et al., 2019).

A conceptual gap remains regarding the effective role of connected natural fractures and faults hosted within basement volumes (intrabasement structures) in an offshore context (Holdsworth et al., 2019). These structures are difficult to investigate offshore because their size is commonly below seismic resolution (Tanner et al., 2020). Consequently, characterising sub-seismic to regional-scale structures, and their potentially long-lived tectonic evolution, requires more than just low-resolution datasets. To mitigate these challenges, analogue onshore basement exposures can be of great assistance as they provide more extensive and ready site access, and data availability from regional to micro-scale resolutions (e.g. regional geophysical data, field mapping, and thin sections).

The island of Smøla, within the Mid-Norwegian passive margin, forms a subaerial exposure of crystalline basement rocks (Figure 1a). The island is an ideal analogue for basement highs offshore Central Norway, owing to both its proximity to the offshore Frøya High, and the similarity of basement geology at both locations (Rønning and Elvebakk, 2005; Slagstad et al., 2011). Smøla has abundant local and regional structures, which document the tectonic evolution of the margin through time. As such, any geological insights from Smøla could then potentially be applied to basement highs offshore, furthering the understanding of their internal structure, and aiding in the reconstruction of their tectonic evolution.

The brittle tectonic evolution of onshore basement exposures along the Norwegian passive margin has been extensively studied (Redfield et al., 2004; Davids et al., 2013; Ksienzyk et al., 2016; Scheiber et al., 2016, 2019; Scheiber and Viola, 2018; Tartaglia et al., 2020; Fossen et al., 2021; Hestnes et al., 2022), with Tartaglia et al. (2023) providing the latest insights for the

Mid-Norwegian portion. Applying the tight constraints from these studies, and a new three-dimensional (3D) perspective from four diamond drill holes on Smøla Island, we present a case study that describes and tests a comprehensive workflow for characterising onshore basement blocks. Our multiscalar approach integrates surface geological tools (outcrop mapping and sampling), petrography, regional datasets (airborne magnetic surveys and digital terrain models (DTMs)), along with K-Ar geochronology to constrain the absolute time dimension of the reconstructed tectonic phases. As fault and fracture arrays in crystalline rocks control local secondary permeability (Gillespie et al., 2020), our work has significant implications on resolving reservoir characteristics associated with offshore basement highs, and basement deformation more generally. This study, therefore, offers a method to generate crucial deterministic inputs for modelling basement fractures and petrophysical behaviour over time.

2 Geological framework

2.1 Regional perspective

Smøla Island, located in Central Norway, is set along the Mid-Norwegian passive margin (Figure 1a), a region shaped by a prolonged and complex geological history (Peron-Pinvidic and Osmundsen, 2020). The island (Figure 1b) is comprised by 445.7 ± 3.8 Ma plutonic magmatic-arc rocks (Tucker et al., 2004; Slagstad et al., 2011) and oceanic crustal units, all of which were emplaced and accreted just prior to the Silurian-Devonian (~430 to 400 Ma) Scandian Phase of the Caledonian Orogeny (Tucker et al., 2004; Gee et al., 2008; Corfu et al., 2014; Slagstad and Kirkland, 2018). Caledonian shortening led to nappe and thrust fault development, with transposition of the Smøla rocks along major detachments over both the allochthonous continental Neoproterozoic Baltoscandian nappes and the underlying autochthonous Palaeo- to Mesoproterozoic Baltican crystalline basement of the Western Gneiss Region (WGR) (Fossen, 1992; Tucker et al., 2004; Corfu et al., 2014)(Figure 1c).

During the Early Devonian collapse of the by then overthickened orogen resulted in significant crustal extension by both reactivation of favourably oriented contractional structures (Fossen, 2010; Fossen et al., 2017) and development of new crustal-scale extensional shear zones, and regional exhumation (Figure 1) (Osmundsen et al., 2006). Devonian extension also caused the Smøla rocks to be translated, in response to both strike-slip and down-faulting across the Møre-Trøndelag Fault Complex (MTFC), a regional fault system with complex kinematics that was repeatedly reactivated through time (Grønlie and Roberts, 1989; Grønlie et al., 1994; Redfield et al., 2004; Watts et al., 2023). Smøla experienced limited metamorphic overprint (on average sub-greenschist facies conditions) and only localised ductile deformation (Tucker et al., 2004). Associated with the Devonian tectonic inversion, extensional (possible pull-apart) basins formed in response to brittle extensional faulting, such as the MTFC-related Edøyfjorden Basin proximal to Smøla (Figure 1b) (Bøe and Bjerkli, 1989; Bøe et al., 1989; Osmundsen et al., 2006; Fossen et al., 2017).

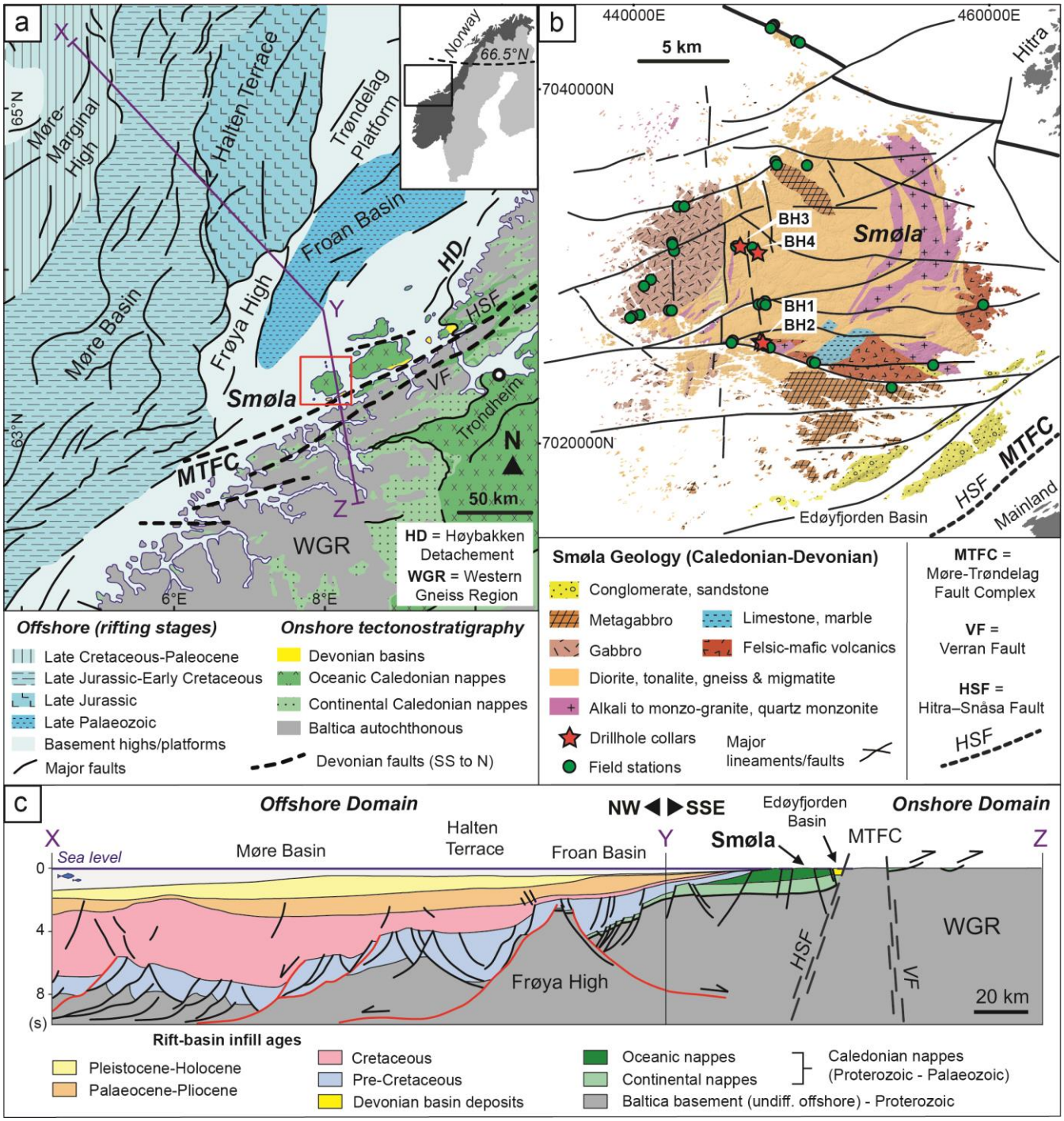

Figure 1. The geological context of Smøla Island, Central Norway. A) Regional setting of Smøla on the Mid-Norwegian passive margin. Smøla is separated from the Western Gneiss Region (WGR) by the Møre-Trøndelag Fault Complex (MTFC), with two fault strands, the Hitra–Snåsa Fault (HSF) and the Verran Fault (VF). The Høybakken Detachment (HD) is shown to the NE of Smøla. Major basins are present are to the NW of Smøla, in the offshore domain (e.g. Møre Basin), bound by normal faults and structural

highs (e.g. Frøya High) (modified from Faleide et al., 2008; Bedrock map of Norway, Geological Survey of Norway, 2021). B) The local geology of Smøla, showing the Caledonian and Devonian geology. Significant lineaments and faults (interpreted from airborne geophysics, DTM, and field studies) crosscut the island, with the MTFC (HSF strand) trace indicated. The drill holes (red stars) and outcrop mapping locations (green circles) are shown (modified from Fediuk and Siedlecki, 1977). C) Onshore-offshore interpretive geological cross section (X-Y-Z) as shown in Panel A, showing major regional structures and crustal anatomy relative to Smøla. Including the two strands of the MTFC (HSF and VF) and the Frøya High offshore (modified from Zastrozhnov et al., 2020).

Post-Caledonian extension and rifting continued to the Late Cretaceous/Early Palaeocene, eventually leading to the Greenland-Eurasia plate break-up at ~54 Ma and opening of the North Atlantic, forming the Norwegian passive margin (Peron-Pinvidic and Osmundsen, 2018; Bunkholt et al., 2022). This prolonged process involved multiple tectonic phases: rift initiation during the Carboniferous, Permo-Triassic crustal stretching and rifting, Late-Triassic to Jurassic crustal thinning, renewed Mid-Jurassic to Early Cretaceous rifting, with extension of the margin during the Late-Cretaceous to Paleocene, and early seafloor formation and spreading during the Paleocene-Eocene (Mosar et al., 2002; Faleide et al., 2008; Peron-Pinvidic and Osmundsen, 2018; Gernigon et al., 2020).

These events produced discrete generations of basins (such as the Froan and Møre Basins) along the newly-forming Norwegian shelf, which progressively infilled with synrift sediments (Figure 1a & c) (Faleide et al., 2008; Zastrozhnov et al., 2020). In places, structural highs of Caledonian-aged and underlying Baltica crystalline basement, such as the Frøya High to the NW of Smøla formed through rift-related exhumation between these basins, leading to a remarkable host and graben series (Muñoz-Barrera et al., 2020). Bounding the structural highs and the different basins, are crustal-scale extensional faults (Figure 1a & c) (Mosar et al., 2002; Skilbrei et al., 2002). Overall, this protracted rifting and extension history resulted in a highly attenuated offshore domain, reactivating, and overprinting the existing Caledonian deformation features (Figure 1a & c) (Mosar et al., 2002; Zastrozhnov et al., 2020).

2.2 The geology of Smøla

Smøla is composed of several Caledonian-aged bedrock types traditionally attributed to the Caledonian Upper Allochthon (Roberts and Gee, 1985) (Figure 1b), including diorite (the most common lithology), gabbro, tonalite, alkali granite, quartz monzonite to monzo-granite, quartz-feldspar and amphibolite-biotite gneiss, limestone and volcanic rocks (andesitic to rhyolitic in composition in a faulted block on the SE-portion of Smøla). Late, felsic to mafic dykes crosscut all other rock types (Fediuk and Siedlecki, 1977; Bruton and Bockelie, 1979; Roberts, 1980; Gautneb, 1988; Gautneb and Roberts, 1989). In addition to the 445.7 ± 3.8 Ma (1σ) U/Pb intrusive age of a dated granodiorite (Tucker et al., 2004), a granitic dyke was dated to 428 ± 10 Ma (2σ) (Rb/Sr) (Gautneb, 1988), providing an Ordovician-Silurian age envelope for the plutonic rocks on the island. To the S and SE of Smøla the Caledonian bedrock is unconformably overlain by the late Silurian-mid Devonian sedimentary cover of the Smøla Group, and later Jurassic-Cretaceous sedimentary successions (Fediuk and Siedlecki, 1977; Bøe and Bjerkli, 1989; Bøe et al., 1989). These include siliciclastic deposits of red-oxidised polymictic conglomerate, siltstone,

and sandstone (Bøe et al., 1989), which fill in Devonian extensional basins (e.g. Edøyfjorden Basin, Figure 1b) along the MTFC (Bøe and Bjerkli, 1989).

Further to the S and SE of Smøla (and bounding the Devonian basins), the ~NE-SW striking MTFC is the most proximal and dominant regional-scale structure to the island. This wide (10 to 50 km) structure extends for >600 km from Central Trøndelag into the northern-part of the North Sea, and branches into two sub-parallel strands, the Hitra–Snåsa Fault (HSF) to the NW (the most proximal to Smøla), and the Verran Fault (VF) to the SE (Figure 1a,b, & c) (Watts, 2001; Olsen et al., 2007; Watts et al., 2023). The structural evolution of the MTFC is complex, with a polyphase deformation history from the Devonian until the Cenozoic (e.g. Grønlie and Roberts, 1989; Seranne, 1992; Watts, 2001; Redfield et al., 2004; Tartaglia et al., 2023; Watts et al., 2023).

3 Materials and methods

This study's multi-technique approach involves a variety of 2D and 3D datasets, ranging from the regional-scale through to the micro-scale. Integrated into these datasets is the absolute time dimension, provided through K-Ar geochronology of structurally well-characterised fault rocks, which give chronological constraints on all other datasets. We briefly outline the methods below, with a more detailed description in the supplementary material.

3.1 Geophysical and remote sensing data and lineament mapping

The geophysical and DTM data used in this study were acquired by the Geological Survey of Norway (NGU) (Nasuti et al., 2015), with details on survey parameters and data processing available in the supplementary material. Our lineament picking and mapping followed White (2014) and Scheiber and Viola (2018), making use of both the magnetic geophysical and DTM imagery within a geographic information systems (GIS) software platform (Figure 2). The description of the methodology used to identify and place the lineaments is also available in the supplementary material.

3.2 Field work and drill hole logging

The field-based structural data acquisition involved standard geological field methods, including the systematic mapping of representative outcrops (Figure 1b) and ground-truthing of possible exposed deformation zones identified in the lineament mapping. In total, sixty-six outcrop sites were studied, with data collected recording deformation feature types, fracture/vein mineral infill, fault slip information, host rock lithology, and cross-cutting/genetic relationships between the various features. The four diamond drill holes used in this study (stored in Trondheim, Norway) were drilled in 2019 and were designed to target major structures, and sample weathered basement rocks. Geological features in the drill cores (Figure 4) were systematically logged downhole (for a total investigated length of 364.9 m of diamond drill core), recording lithology and rock alteration, deformation types, fracture/fault characteristics, mineral infill, and cross-cutting relationships. These data were also

used for the 3D modelling of intersected deformation zones in drill holes BH1 and BH2 (Figure 8). The methodology used to measure structural data in drill core followed both the methods of Holcombe (2013) and Blenkinsop et al. (2015). A more detailed description of the methodology is available in the supplementary material.

3.3 X-ray diffraction and K-Ar dating

Seven structurally controlled fault gouge and breccia samples (Figure 9) were collected from fault and deformation zones in both drill core and outcrop, and subsequently processed at the NGU laboratory in Trondheim, Norway. Initially, all samples were disintegrated and separated into <0.1 µm, 0.1-0.4 µm, 0.4-2 µm, 2-6 µm, 6-10 µm size fractions. Each of these size fractions then underwent quantitative analysis for both potassium (K) and argon (Ar) using total digest ICP-OES, and a Isotopx NGX multi collector noble gas mass spectrometer system respectively. X-ray diffraction (XRD) analysis was performed on each fraction to determine and quantify the mineralogical composition. A full description of both the XRD and K-Ar analysis methodology is available in the supplementary material and in Viola et al. (2018).

4 Results

4.1 Lineament mapping from geophysics and DTM data

The analysis of regional-scale features such as geophysical lineaments and topographic features (Figure 2) formed the initial stage of the study. These features occur on the kilometre-scale, and using both geophysical and DTM imagery, can be traced over both off- and onshore areas. The >2000 mapped lineaments (available within the supplementary data repository) are linear, curvilinear to irregular features which either crosscut or terminate against one another (Figure 2a & b). The lineaments are classified based on length and hierarchy of formation: First-order lineaments are potentially major regional structures; second-order lineaments, commonly >10 km in length, are typically major splays or secondary features off the first-order lineaments; while third-order lineaments, typically <10 km in length, constitute the remaining lineaments.

The first, second, and third-order lineaments are sub-divided into eight orientation trends, which are labelled: L1) N-S, L2) NW-SE, L3) E-W, L4) ENE-WSW, L5) NE-SW, L6) WNW-ESE, L7) NNE-SSW, and L8) NNW-SSE (Figure 2b) (hereinafter as L1 to L8). Determining precise cross-cutting relationships between these lineament trends is often challenging due to imagery resolution and defining lineament end points. However, where possible, interpretive cross-cutting relationships can provide a relative timing of lineament formation. The age, cross-cutting, and termination relationships of the specific lineament trends are summarised in Table 1, and selectively illustrated by colour in Figure 2b.

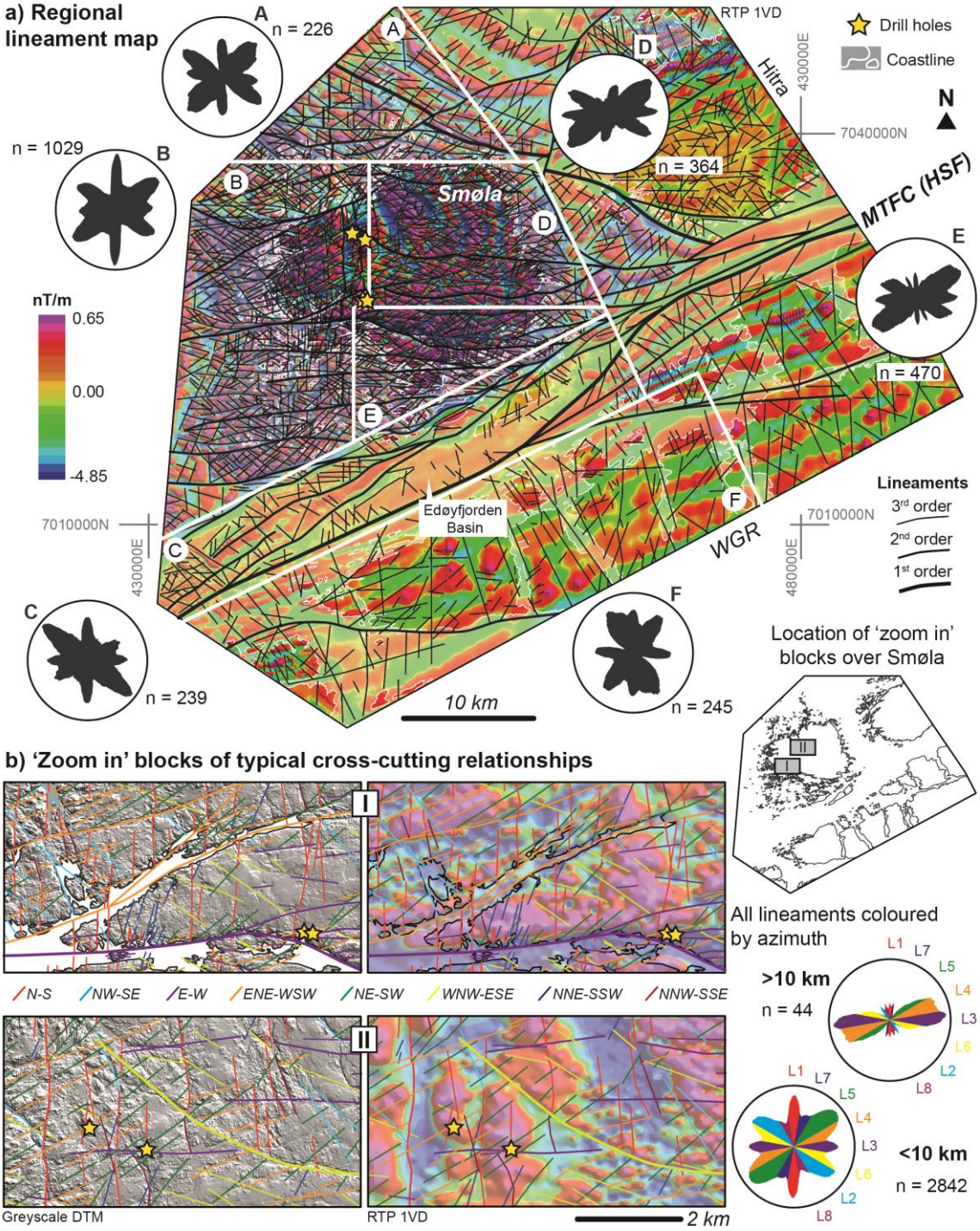

Figure 2. A) Airborne magnetic survey imagery (reduced to pole-first vertical derivative (RTP-1VD)) over Smøla Island and surrounding areas (coastline shown in white). Displayed over the magnetic imagery are first, second, and third-order lineaments mapped from both the magnetic data and DTM data. Airborne magnetic survey imagery from Nasuti et al. (2015). The area over Smøla onto the WGR region is sub-divided into A (north of Smøla), B (western and SW of Smøla), C (area over the MTFC), D (NE

Smøla), E (SE Smøla), and F (WGR area). Rose plots of strike trends of mapped lineaments are shown by area. B) 'Zoom in' blocks showing representative examples of cross-cutting relationships between the different lineament trends (coloured by trend) on both DTM and geophysical imagery (DTM data from the NGU). Locations of the 'zoom in' blocks are displayed on the adjacent schematic map of Smøla (coastline map courtesy of the NGU) along with rose diagrams showing orientation trends of lineaments with >10 km and <10 km lengths. Rose plots are coloured the same as the lineaments on the 'zoom in' blocks and are labelled to show the L1 to L8 lineament trends.

Table 1. Interpretive age relationship matrix between the main lineament trends. The lineament trends are ordered as they are discussed in the text. Relationship types include X = cross-cutting, T = terminating, ? = uncertain.

	Lineament trends	*Younger* N-S	NW-SE	E-W	ENE-WSW	NE-SW	WNW-ESE	NNE-SSW	NNW-SSE
Older	L1 N-S		X	X	X	X	X	X	X, T
	L2 NW-SE	X		X	X	X	X	X	X, T
	L3 E-W		X		X	T	X	T, X	X, T
	L4 ENE-WSW			X		T	X	X?	X
	L5 NE-SW		T, X				T	X, T	X, T
	L6 WNW-ESE			X		T		T	X?
	L7 NNE-SSW			X	X				X?
	L8 NNW-SSE		X					X?	

L1 is most common in the western part of Smøla and offshore in areas A and B on Figure 2a. These lineaments are typically second- to third-order, are crosscut by all other lineaments, except for L8 which, in places, terminates against L1 (Figure 2b.I). As there are local mutual cross-cutting relationships, L1 and L2 are likely coeval or conjugates. L1 and the L3, L4 lineaments have complex cross-cutting relationships, with L1 being potentially horizontally offset (dextrally and sinistrally) with multiple possible reactivations in places (Figure 2b.I & b.II).

L2 is common to the north of the MTFC, over most parts of Smøla and offshore (areas A, B, D, and E on Figure 2a). L2 is similarly crosscut by many of the other lineaments (Figure 2b). L2 crosscuts L3 and the L5 lineaments, as well as the magnetic grain (Figure 2b), but this may be due to later reactivations. The L2 and L8 lineaments have rare mutual cross-cutting relationships, but otherwise L8 tends to terminate up against L2.

The L3 lineaments are most common in central Smøla, particularly in areas B, D, and E, clustering on the NW side of the MTFC (Figure 2a). L3, mostly occurring as second-order lineaments and possible splays off the first-order MTFC (HSF) lineament (Figure 2a), are cross-cut by L2, L7 and L8 (Figure 2b.II). L3 also exhibits mutual cross-cutting (potentially coeval) relationships with L4 (which in turn typically splay off the E-W structures) (Figure 2b.I). Frequently, L1, L2, and L3 (third-order lineaments only) are similarly crosscut by the same lineament trends, indicating that the L1-L3 lineaments may have

formed coevally (Figure 2b.II). The longer L3 second-order lineaments do however crosscut most other lineaments (Figure 2b.I), suggesting either a later formation or a longer period of activity/reactivation.

The L4 and L5 lineaments are pervasive across Smøla within areas A, D, E, B, and F (Figure 2a). These lineaments are typically third-order lineaments and sub-parallel to the MTFC (HSF) trend. In the eastern part of Smøla (areas E and D), they cluster on and terminate against the N/NE sides of L3 (Figure 2b.I), possibly representing third-order Riedel shears or splays off the second-order L3. In the western part of Smøla they form prominent elongate topographical valleys in the DTM and terminate less commonly against L3. These lineaments crosscut and dextrally offset both the L1 and L2 (less distinctly) and terminate against L3 and L6 (Figure 2b.II). L4 and L5, however, are either locally crosscut by, or are terminated up against by L6, L7, and L8 (Figure 2b.II).

L6 is present throughout the study area, although mostly NW of the MTFC, and are either second or third-order lineaments. L6 crosscuts all other lineaments, with only rare examples of L7 and L8 crosscutting it (Figure 2b.II). In places, an apparent late reactivated L2 displays similar mutual cross-cutting relationships as L6. The two least common lineament trends, L7 and L8, are most abundant in the areas D and B (for L7), and areas F and E (for L8) over Smøla and the WGR. L7 and L8 mutually crosscut one another, although this is mostly seen in area F (Figure 2a). Overall, these lineaments terminate against and crosscut all the other lineaments (Figure 2b.I & b.II), suggesting an early formation and a possible late reactivation.

4.2 Field, drill hole, and petrographic results

Field observations (Figure 1b) and four diamond drill holes (Figure 1b & Figure 4) offer a novel 3D perspective on Smøla's geology. Various minerals decorating fracture surfaces, fault rocks, and veins are systematically documented, showing coeval or crosscutting relationships, and orientation trends. (Figure 3, 5 & 6). As such, assemblages of coeval infill minerals have been used to group the deformation features based on the relative timing (summarised and labelled D_1 to D_5 in Figure 7). The coeval mineral assemblages, with corresponding consistent deformation styles and orientation trends, may represent distinct mineralisation events associated with discrete deformation episodes (e.g. Drake et al., 2009; Viola et al., 2009).

We now systematically describe the progressive deformation and mineralisation types starting from the apparent earliest to the latest features. As a part of the structural characterisation, we have included both the field and drill hole structural data (Figure 3). However, the drill hole data were localised in specific parts of the island and biased towards including shallowly dipping features (e.g. Terzaghi, 1965). Therefore, field data primarily inform the structural descriptions, as they illustrate typical geometries and kinematics across Smøla.

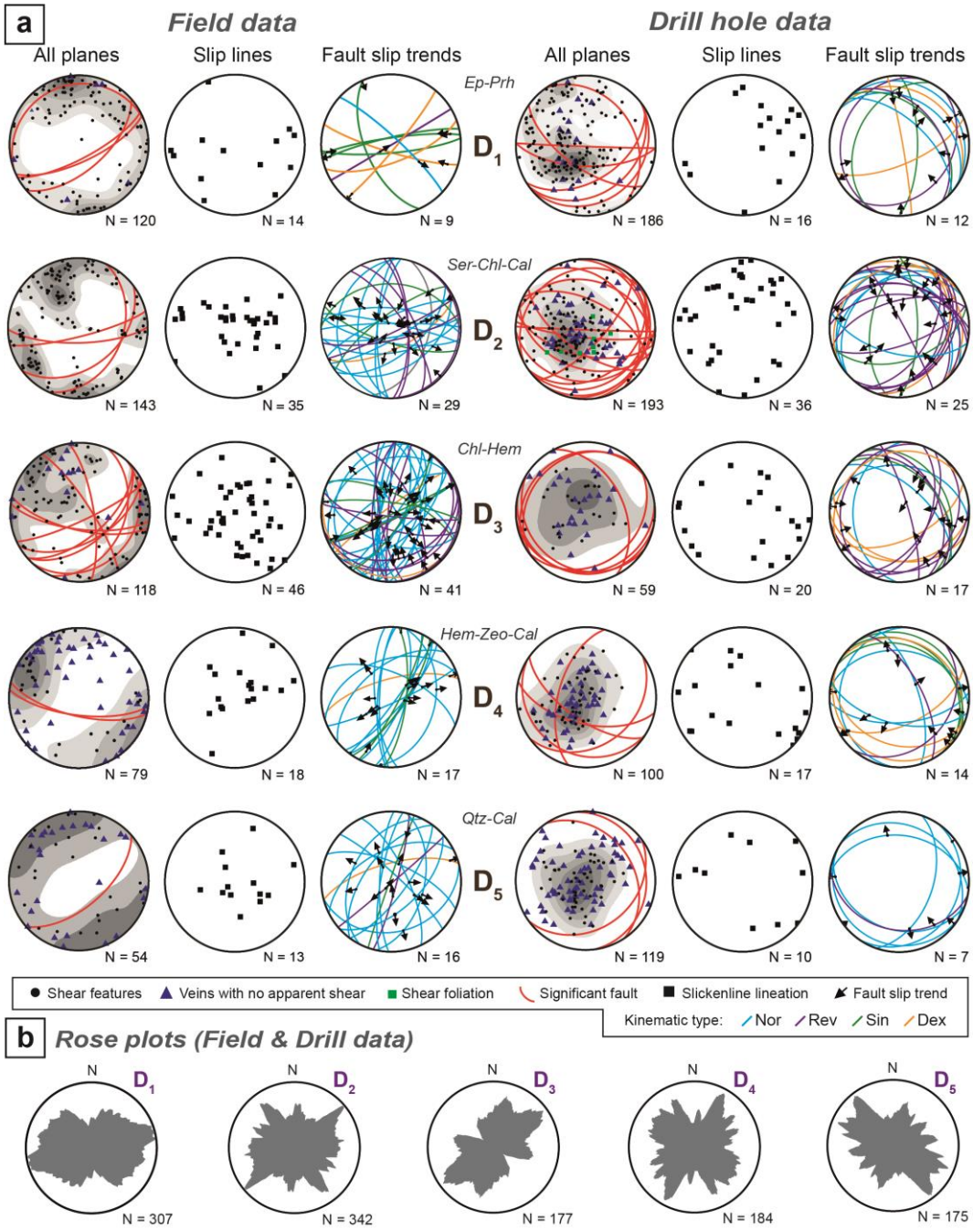

Figure 3. A) Equal area, lower hemisphere stereonet plots of deformation features in outcrop or drill core, sorted by deformation episode D_1 to D_5, and coeval mineral assemblages. All plane plots Kamb contoured at 2σ interval, with drill hole stereonets not Terzaghi corrected. B) Rose plots showing strike orientation trends (frequency) of all features (combined outcrop and drill core) by deformation episode. Mineral types: Ep=epidote, Prh=prehnite, Ser=sericite, Chl=chlorite, Cal=calcite, Hem=hematite, Zeo=zeolite, Qtz=quartz. Kinematic types: Nor=normal, Rev=reverse, Sin=sinistral, and Dex=dextral.

4.2.1 D_1: epidote-prehnite-stable faulting and veining

The earliest recognised brittle deformation features on Smøla are epidote and prehnite veins, hydraulic breccias, and cataclasites involving at least three different generations of epidote (Ep 1, 2, & 3 on Figure 5a & b). Field data reveal two clusters of the shear fractures and veins: one striking ENE-WSW with steep SSE dips, and the other NW-SE with steep NE dips. Major structures associated with fault rocks (red great circles on the 'All planes' plots on Figure 3), primarily strike ENE-WSW with steep SSE dips. Slip lineations show varied orientations but have moderate to shallow plunges, trending E or W. Kinematically, most structures with slip-trend information exhibit strike- to oblique-slip motion, predominantly oriented E-W. Overall, the data suggest a sinistral strike-slip regime with NNE-SSW contraction and WNW-ESE extension. Drill data also exhibit similar strike orientations, with an additional trend NW-SE dipping shallowly NE. Kinematically, shear features are mostly normal, dipping moderately to shallowly NE, indicating a mean NE-SW extension direction.

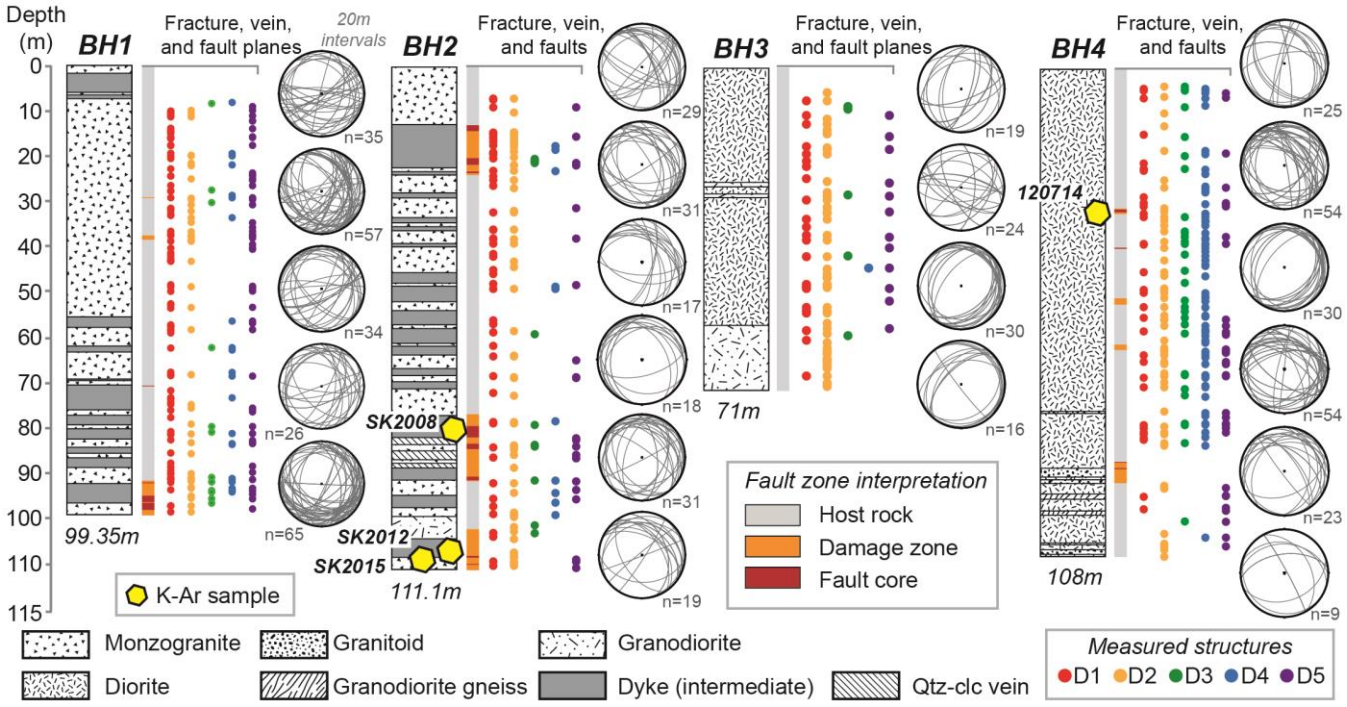

Figure 4. Graphic logs showing both downhole lithology and fault zone interpretations for each of the four Smøla diamond drill holes. Measured structural data are shown distributed downhole, grouped by mineral assemblage (and deformation episode), with D_1 = epidote-prehnite, D_2 = sericite-chlorite-calcite, D_3 = chlorite-hematite (+/- calcite), D_4 = hematite-zeolite-calcite, and D_5 = quartz-calcite. Measured structures are also represented plotted as planes on the adjacent stereonets. Each stereonet represents at least 20m of drill core and correspond to the downhole depths of the drill holes.

The epidote mineralisation consists of early pale/light green-yellow (Ep 1 and 2) or a later grass-green type (Ep 3). Early epidote typically infills tensile or shear veins, with well-developed slickenside surfaces on the vein-host rock interfaces or

internally on crack-seal surfaces (Figure 5a). In contrast, later grass-green epidote occurs as infill of irregular, bifurcating to anatomising veins (Figure 5b), which in places crosscuts and reworks the early epidote. All three types cross-cut host rock lithological features, such as aplitic veins.

Prehnite veins, significantly less common than epidote veins, occur in drill holes BH1 and BH2 together with epidote. Prehnite typically pale grey-green, infills veins, and can form dense networks grading to dilatant hydraulic breccias (Figure 5a, drill core). In the case of the hydraulic breccias, included fragments are either host rock fragments of polycrystalline aggregates of quartz-feldspar or reworked epidote cataclasites/veins (in places with host rock fragments with included veins; Figure 6c).

The earlier epidote locally forms the matrix mineral of at least two generations of cataclasite to ultracataclasite, which are associated with the major structures on Figure 3a. The earliest epidote cataclasite to ultracataclasite (Ep 1) is typically preserved as isolated fragments (1-5 mm in size), which possibly originated as thin discrete pockets with a weak to distinct foliated to banded matrix dominated by very fine-grained epidote and clay (forming up to 75 %-90 % of the pockets). The included clasts are fine-grained (average size <60 µm), poorly sorted and subangular, and are typically mono- to polycrystalline aggregates of quartz-feldspar host rock (Figure 6a & b). The later epidote cataclasite (Ep 2) occurs as localised zones (typically <10 cm in width), with a massive matrix (making up 60 %-70 % of the zones) formed by fine-grained epidote and clay (Figure 6b). The included fragments are very fine- to coarse-grained (10 µm-6 mm), poorly sorted, angular- to sub-angular, and polycrystalline fragments of host rock (quartz-feldspar) or reworked fragments of the earlier epidote ultracataclasite. The included Ep 1 and host rock fragments within the Ep 2 cataclasite exhibit minor offset and rotation from each other, suggesting that there was limited to no rigid-body rotation and mechanical comminution of the fragments.

Rarely, prehnite ultra-cataclasites occur as discrete zones 3-5 cm in width, striking NNW-SSE and NW-SE, with shallow to moderate dips (30°-65°) (Figure 3a, drill data). Prehnite comprising >90 % of the matrix of these zones, is very fine-grained, with interspersed clay. The included clasts are fine-grained (<50 µm-1 mm), moderately sorted, subrounded to angular, and made up of mono to polycrystalline fragments of host rock and epidote cataclasite. The prehnite ultracataclasites are associated with the epidote cataclasites, with both the cataclasites mutually reworking one another.

4.2.2 D_2: repeated sericite-chlorite-calcite faulting

D_2 sericite-chlorite-calcite shear features (Figure 5e) invariably rework D_1 structures. These structures occur as single shear fractures or dense networks and local brittle-ductile shear zones.

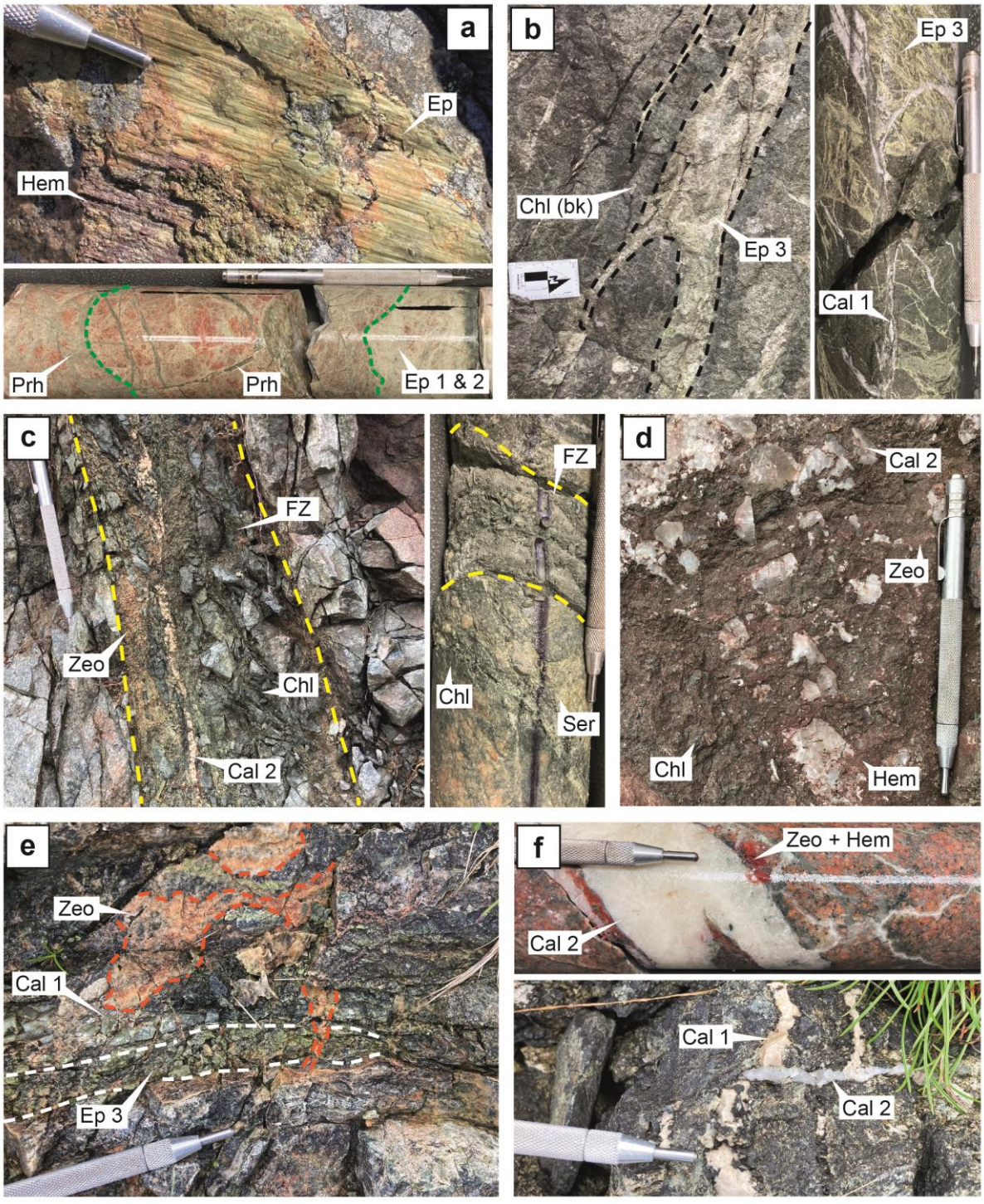

Figure 5. Representative examples of mesoscale deformation features on Smøla. A) Epidote slickenside surface (combination of light green and grass-green epidote) and light green epidote (Ep 1 and 2) veins and cataclasite being cross-cut by prehnite (Prh) vein

breccia in BH1. B) Bifurcating diffuse veins of grass-green epidote (Ep 3) with black chlorite (Chl (bk)); core-hosted abundant grass-green epidote veins are cross-cut by early calcite veins (Cal 1). C) Chloritic (Chl) fault zone (+/- sericitic) with later zeolite (Zeo) and calcite vein (Cal 2). The zone is highly fractured, the friable gouge (left side of the zone) represents a fault core; a similar narrow fault zone in BH2, with strong foliation and abundant sericite (Ser) infill. D) Chlorite (Chl)-hematite (hem) cataclasite veneer on a fault surface with a later zeolite overprint and late quartz (Qtz)-calcite (Cal 2) infill. E) Zeolite (Zeo) veins cross-cutting early calcite (Cal 1) and epidote (Ep 3) veins. F) Deformed early calcite veins (pale brown coloured) (Cal 1) being cross-cut by translucent white late quartz-calcite vein (Cal 2). A-F) Scratch pen for scale = 13 cm, B) Scale bar arrow = 10 cm.

Field data reveal three main trends of the shear fracture orientations (Figure 3a): E-W to ENE-WSW striking, steeply to moderately S dipping; NE-SW striking, moderately SE dipping; and NNW-SSE striking, steeply E dipping. Slip lineations mostly plunge steeply, indicating dip-slip kinematics, with shallower trends toward W or SE. Kinematically, most shear features exhibit normal or oblique-normal shear-sense, striking E-W or NE-SW. Some N-S striking, steeply E-dipping reverse faults are also observed. Sinistral and dextral strike- to oblique-slip features strike E-W, dipping moderately N or S. Overall, these features indicate an extensional regime with a mean NW-SE extension direction. Drill data show predominantly NW-SE striking, shallowly NE dipping fractures and veins. Major structures mostly dip shallowly SE, with steeper dipping features striking E-W. Kinematically, shear features are mostly reverse, dipping SE or NE, with some normal and strike-slip features.

The well-developed deformation zones, with locally foliated gouge with highly fractured and disaggregating host rock clasts and early deformed calcite veins (Figure 5c) are typically oriented the same as the first two shear fracture outcrop trends (Figure 3a). D_2 structures, especially the well-developed deformation zones, are almost phyllitic at the microscale (Figure 6d & E), locally involving fine to medium-grained sericite/muscovite (30-40 %), chlorite (30 %), and clay (>5 %), with elongate domains of fine-grained recrystallised quartz (>20 %; the matrix forms ~80 % of the total volume). The host-rock clasts within this groundmass are 20 µm-1 cm monocrystalline quartz fragments or polycrystalline aggregates of subrounded quartz and altered feldspar.

Microstructural relationships indicate at least two distinct deformation events: an early event with localised shearing along axial planar cleavages in an early folded sericite groundmass with calcite veins (Figure 6d); and a subsequent event, reworking and rotating the earlier axial planar cleavage shear planes (S-surfaces) by later C'-planes. This resulted in the development of an extensional crenulation cleavage (ECC)-type fabric (Figure 6e) (e.g. Passchier and Trouw, 2005). These ECC zones also rework D_1 epidote cataclasite and fragmented host rock. The host rock fragments locally form σ porphyroclasts with very fine-grained quartz in the strain shadows, and the sericite-chlorite groundmass (and very fine-grained clay) deflected around them.

4.2.3 D_3: chlorite-hematite-decorated fault rocks and shear fractures

The D_3 chlorite-hematite structures (Figure 5d), involve brown-red staining or 'dusting' of hematite and chlorite decorating and infilling these structures. D_3 structures occur as individual anastomosing shear fractures, which locally have hematite slickensides, grading to networks, and breccias and gouges (and possible cataclasites).

Field data show four trends of these shear fractures: NE-SW striking, steeply SE dipping; N-S striking, subvertical to steeply W dipping; NE-SW striking, shallowly SE dipping; and WNW-ESE striking, steeply SSW dipping. Tensile veins mostly strike ENE-WSW and dip moderately to steeply SSE. Major D_3 structures (with breccia and gouge) are sub-parallel to these trends. Slip lineations vary, with steep dip-slip predominating and shallower strike-slip orientations trending NE, W, and SW. Kinematically, shear features are mainly normal to oblique-normal, striking NNE-SSW, with shallow S-dipping thrusts and vertical N-S striking reverse faults. Sinistral strike-slip features strike ~ENE-WSW, with occasional dextral features striking NE-SW. These features suggest associated WNW-ESE to NW-SE extension. Shear fractures and veins from drill data, primarily strike ENE-WSW and dip shallowly SE. Major drill core structures have shallow dipping geometries, either S or NW. Shear features are predominantly dip-slip and reverse, dipping either ~E or NW, with some dextral features striking E-W to NE-SW. Overall, these structures suggest a mean NW-SE contraction.

The chlorite-hematite breccias to gouges, typically diffuse zones (up to ~3 m thick), exhibit abundant D_3 fractures forming damage zones around them. The gouges are indurated and are moderately to well consolidated features in hand specimen (Figure 5d). These features at the microscale are cemented by chlorite (40 %), hematite (30-50 %), and clay (10-20 %), with the matrix forming 5-20% of the overall zones (rarely up to 60 %; Figure 6f). The chlorite grains, either overprinting or as growths between the fragmented host rock (and host rock clasts), form elongate grains in places. The hematite cement is dark red-brown to opaque in PPL, with the staining/ 'dusting' occurring as very fine-grained particles within fractures/matrix and overprinting the host rock. The host rock clasts themselves are typically medium- to coarse-grained in size (2 mm-1 cm), moderately to poorly sorted, clast-supported, and comprised by altered quartz-feldspar (feldspar is partially altered to sericite) polycrystalline fragments. Elsewhere, the D_3 structures are associated with thin pockets of hematite-rich foliated to banded cataclasite/indurated gouge (<2 cm in thickness; Figure 6h), with a very fine-grained matrix (up to 80% of the zone) comprised of hematite (80%), clay (15%), and chlorite (5%), with incorporated fine-grained (20-600 µm), poorly sorted and sub-rounded host rock clasts.

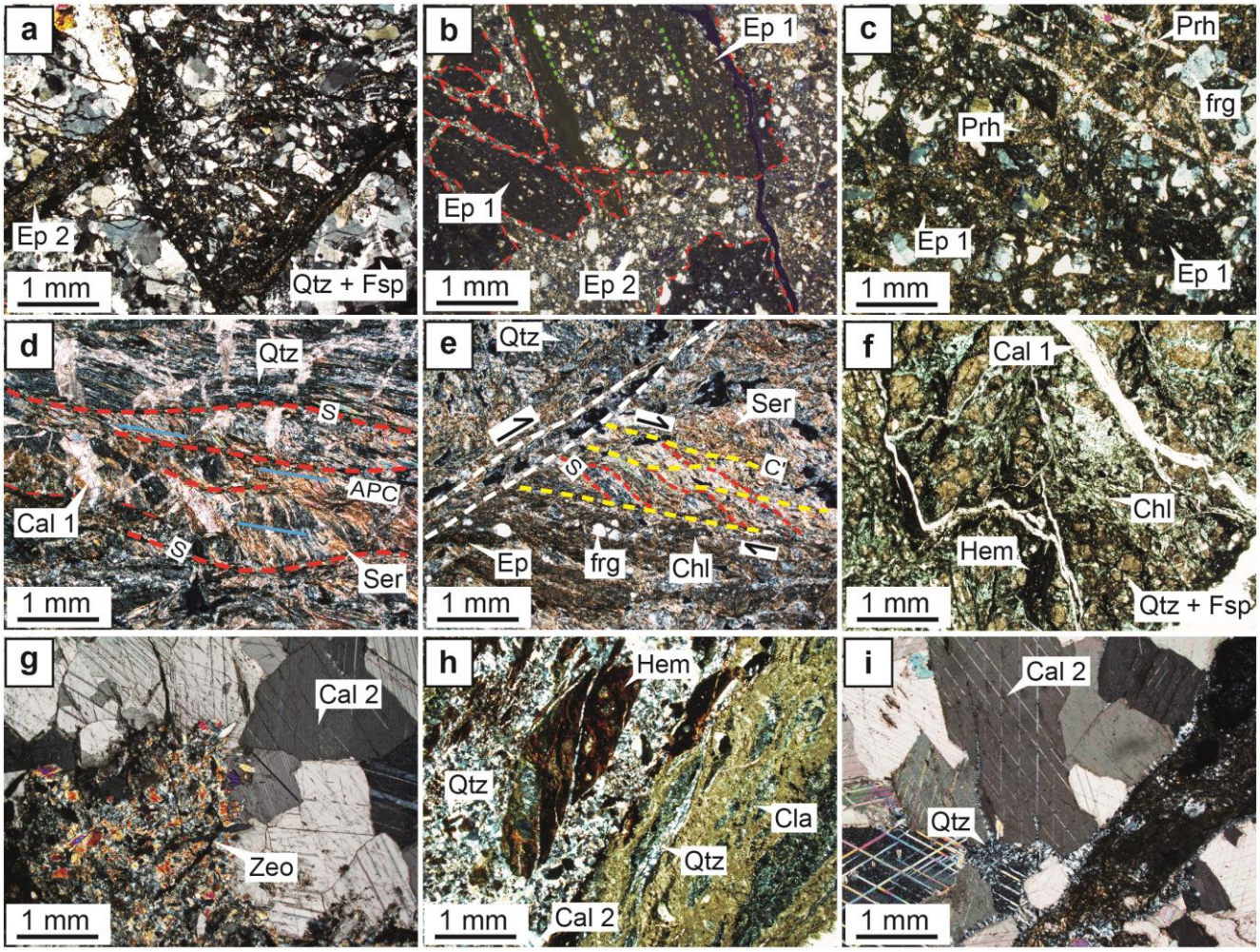

370 **Figure 6. Photomicrographs outlining the progressive deformation episodes affecting Smøla over time. A) An Ep 2 vein and cataclasite reworking host rock monzogranite; B) Two generations of light green epidote cataclasites, an earlier ultracataclasite (Ep 1) fragments, almost isotropic, banded to foliated (green dashed lines highlighting the foliation), set within a later cataclasite (Ep 2). C) Prehnite (Prh) hydraulic breccia and veins reworking Ep 1 cataclasite/veins and host rock fragments (frg). D) Asymmetric folds in a sericitic fabric, and early calcite veins. Associated with the folds, a**
375 **rootless axial planar cleavage has formed (blue lines), along which a later foliation (red lines). E) Possible extensional crenulation cleavage ECC fabric reworking the fabric since in D, forming in a sericite-chlorite shear zone. C'-planes (yellow lines), associated to chlorite, have formed inclined to a main shear surface (white line), and are reworking and back-rotating the cleavage-related foliation (from D), forming S-surfaces. Reworked host rock fragments are also present associated with the C'-planes, and chlorite. F) Chlorite-hematite breccia to gouge with deformed early calcite**
380 **veins (Cal 1), and highly altered host rock minerals (feldspars). G) Zeolite-calcite (+/- interstitial hematite in the zeolite) relatively undeformed vein, with the zeolite crystals subhedral to euhedral crystal faces within the calcite. H) Hematite**

indurated gouge reworked by a later quartz-calcite vein. Abundant clays are adjacent to the vein. I) Late quartz-calcite vein (Cal 2), exhibiting calcite twinning (low deformation overall). All photomicrographs are 2.5x, XPL, except for F, which PPL.

4.2.4 D_4: hematite-zeolite-calcite veining

The D_4 hematite-zeolite-calcite structures, mostly tensile veins (0.1-6 mm in thickness) (Figure 5e & f), crosscut the earlier epidote, sericite-chlorite-calcite (Cal 1), and chlorite-hematite structures. D_4 veins are pervasive across Smøla (Figure 5e & f, drill core), along with rare examples of hydraulic breccias and shear fractures with slickenside surfaces.

Field data indicate the tensile veins strike ~ENE-WSW, dipping steeply SE or NW. Shear fractures primarily strike NNE-SSW to NE-SW with moderate to steep ESE dips. The D4 major structures (breccias and gouges) strike WNW-ESE, steeply dipping SSW. Slip lineations typically plunge steeply, showing dominant dip-slip, with subordinate shallower strike-slip lineation orientations ~NE/SW. Kinematically, features are mainly normal shear-sense, striking NE-SW, with minor sinistral strike-slip (NNE-SSW strike) and rare dextral strike-slip (ENE-WSW strike) features, possibly representing conjugate features. This suggests NW-SE extension with NE-SW contraction. The drill data indicate shallow NE-dipping fractures and veins, with major structures striking NW-SE or NE-SW (steeper dipping). Kinematically, these features are mostly moderately dipping oblique- to strike-slip, with sinistral features dipping NE and dextral features dipping SW. Subordinate normal features dip moderately to steeply SSW or ENE. Overall, this indicates a mean ~NNE-SSW extension direction.

Along with zeolite, hematite typically occurs as a bright-red type (different from the D_3-related hematite), along with a later less deformed type of calcite (Cal 2) (Figure 7). In outcrop and in drill core, D_4 structures are associated with coarse-grained 'sugary' masses of zeolite-calcite, locally mineralising over pre-existing veins of epidote or chlorite-hematite (Figure 5e). At the microscale, the D_4 veins consist of zeolite (laumontite) occurring as fine to medium-grained, decussate, subhedral prismatic crystals, in places with interstitial Fe staining. Locally, where zeolite crystals have intergrown with late calcite, they form bounding comb-type textures with euhedral crystal morphologies (Figure 6g). Additionally, radial masses of zeolite occur as grain boundary growths within the calcite portions of the veins, indicating the coeval mineralisation of both minerals. The zeolite, hematite, and late calcite (Cal 2) components in these veins show little to no significant post-crystallisation deformation, implying the D_4 veins are indeed relatively late.

4.2.5 D_5: quartz-calcite veining

The D_5 quartz-calcite veins, involving the late calcite variety (Cal 2) and mineralised quartz, rework and offset all other deformation features (D_1 to D_4) (Figure 7).

The shear fractures and veins in outcrop strike NE-SW, dipping steeply SE or moderately NW. Major structures strike the same but dip more moderately SE. Slip lineations are mainly dip-slip, plunging steeply, with shallow strike-slip lineation orientations toward NNE and ENE. Kinematically, the features have predominantly normal shear-sense, and NE-SW striking. The sinistral and dextral strike-slip planes, possibly conjugates, are oriented similarly to the normal features. Overall, the geometries and kinematics indicate a mean ~E-W extension orientation. In drill core, fractures and veins show a dominant NW-SE strike, shallowly dipping NE. Tensile veins strike similarly NW-SE but with shallow to steep NE or SW dips. Major structures are subparallel to the fracture trends. Kinematically, most features are shallowly NNE/SSW-dipping, WNW-ESE to NW-SE striking normal dip-slip features, indicating a mean NNW-SSE/N-S extensional direction.

The D_5 quartz-calcite veins, in outcrop or drill core, are translucent to opaque white, exhibit crack-seal layering parallel to the vein-host boundary and are planar to bifurcating features (Figure 5f). The veins occur as singular narrow to wide veins (0.1 mm-22 cm) or complex vein networks, and in places, hydraulic breccias with included angular fragments of the host rock. Commonly, these late veins are within and subparallel to existing deformation features, such as sericite-chlorite deformation zones, and may represent a later tensile reactivation of these features (exploiting mechanically weak planes) (Figure 5d). The late quartz-calcite veins crosscut the earlier calcite veins (Cal 1; Figure 5f), which are less quartz-rich, relatively massive, more opaque white, and possess deformed non-planar morphologies to disaggregated irregular domains (for example in D_2).

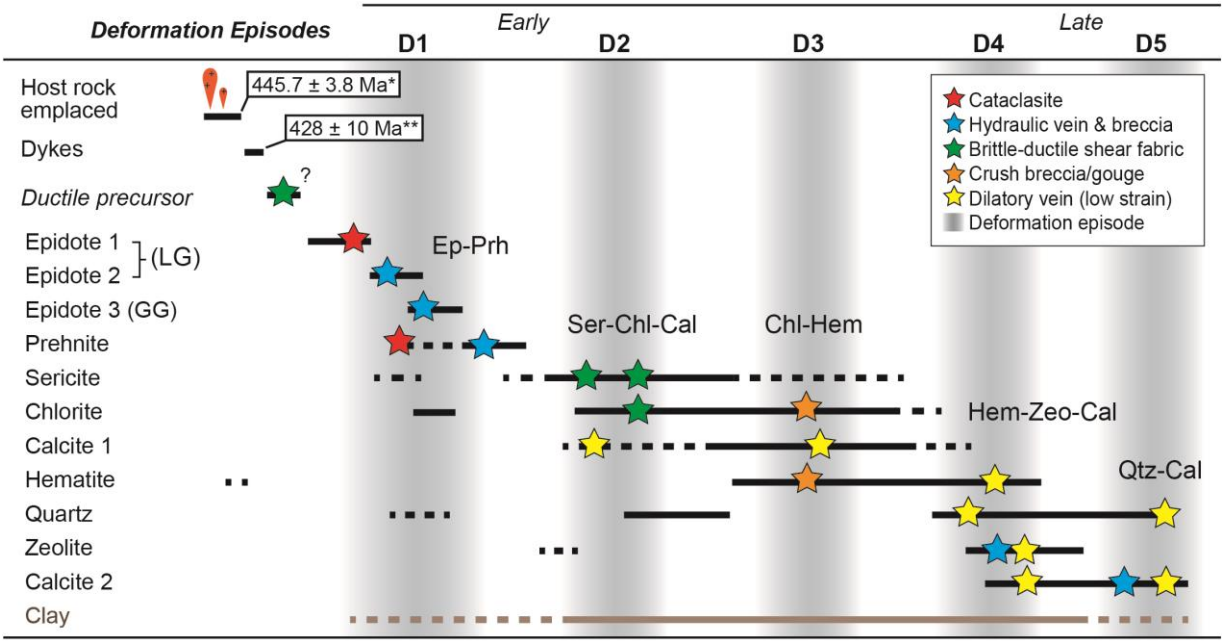

Figure 7. Chronological table of showing relative mineralisation times of different mineral types, key deformation features associated with each mineral type is shown in relative chronology, with clustering of mineralisation and deformation features grouped into five main deformation episodes. These episodes are associated with specific mineral assemblages. Mineral types: Ep=epidote,

Prh=prehnite, Ser=sericite, Chl=chlorite, Cal=calcite, Hem=hematite, Zeo=zeolite, Qtz=quartz. *Host rock age provided by (Tucker et al., 2004); **Age of dyke emplacement by Gautneb (1988).

At the micro-scale, D_5 veins exhibit medium to coarse-grained calcite crystals, typically anhedral, with distinct cleavage, or show fine-grained rims on the quartz grains and between adjacent calcite grains (Figure 6i). In places, coarser-grained quartz form comb-type textures with euhedral crystal terminations into the larger calcite crystals. Commonly, quartz and calcite also mineralise as vein border-parallel alternating bands, indicating multiple crack-seal mineralisations. Finally, while these veins exhibit minimal post-mineralisation deformation (like D_4), the calcite in the veins is twinned, suggesting some later strain.

4.4 Basement deformation in 3D

The four oriented drill holes (Figure 4, with locations on Figure 1b) provide a 3D view of Smøla's geology. Using Leapfrog Works (Seequent, 2022) 3D modelling software, we could delineate the hangingwall and footwall boundaries of deformation zones using logged downhole intersections and orientation data. Implicit volumes were then generated to reproduce the actual thickness, orientation, and extent of zones through 3D space. The modelling of different zones in one volume provides insights into the continuity and extent of deformation zones, as well as potential fracture connectivity. Furthermore, by incorporating both relative (Figure 7) and absolute deformation ages (Figure 11b), the modelling also includes a temporal dimension.

In this study, we have specifically used drill holes BH1 and BH2 for the modelling. These drill holes are close enough together to allow confident correlations between the drill holes. These drill holes intersected deformation zones, veined intervals, and shear zones/fault cores (Figure 4). Considering the geological and deformation characteristics of each of these zones, particularly the fault core intersections (assumed to have the greatest strike continuity) and the associated damage zones, we have correlated at least four zones between the drill holes. The correlations and modelling also used the orientations of bounding deformation features to resolve the geometries of these zones. Examples of modelled zones which are correlated between BH1 and BH2 (labelled I-IV in Figure 8a) are the following:

I) BH1 (37.46 m-37.81 m) and BH2 (12.94 m-23.59 m) intersect a S-dipping E-W striking zone characterised by early D_1 epidote veins and hydraulic breccia (Ep 2) crosscut by D_2 chloritic/sericitic fractures and breccia, and late D_5 quartz-calcite veins (Cal 1 and Cal 2).

II) Both BH1 (70.6 m-70.77 m) and BH2 (79.39 m-81.78 m) intersect a NE-SW striking NW-dipping zone, which widens in BH2, involving early D_1 epidote veins and later chlorite-hematite (D_3) breccia, with stronger hematite mineralisation in BH2. The zone also features deformed early calcite veins (Cal 1).

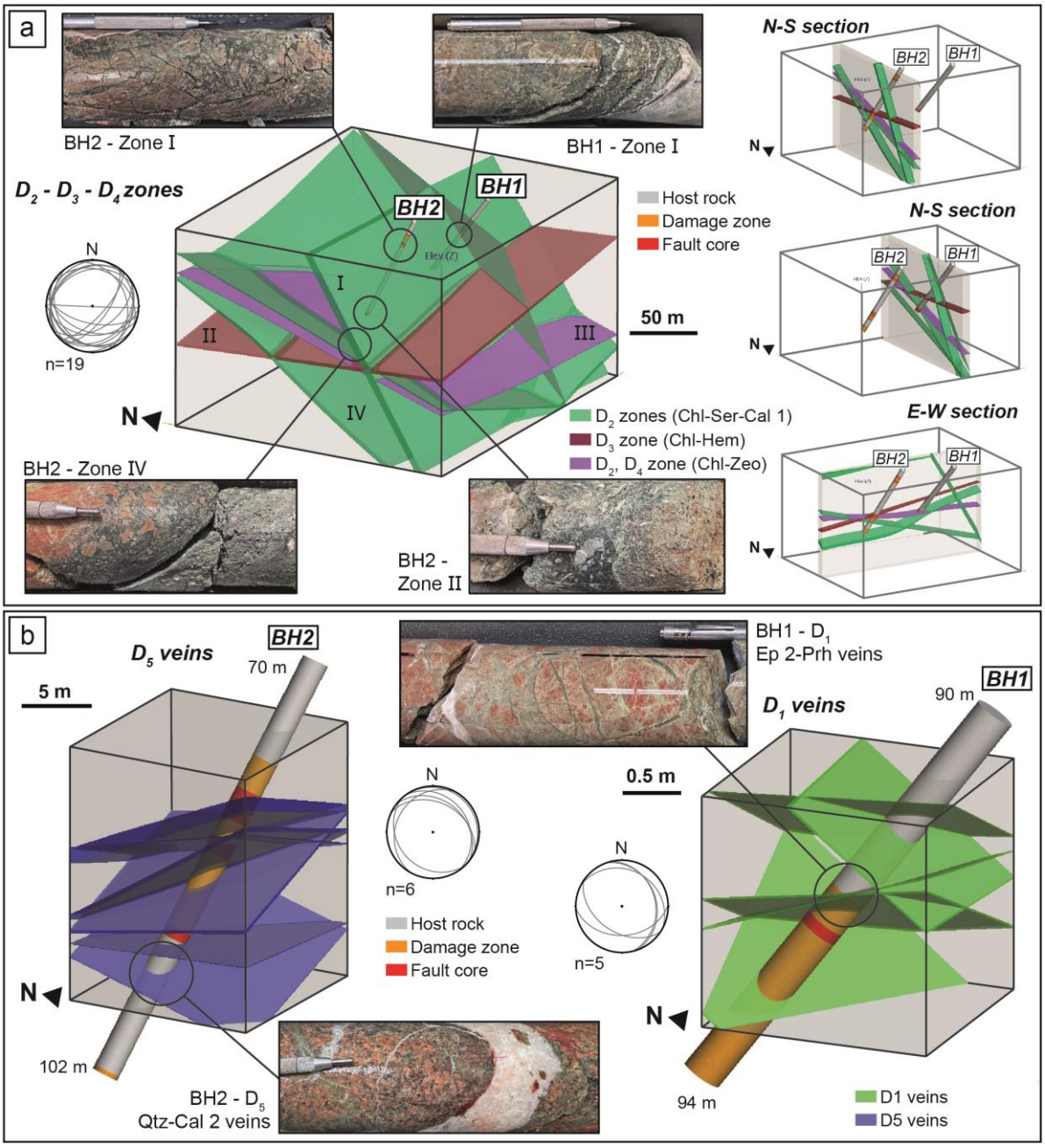

Figure 8. A) 3D model of major intersected brittle structures (green, red, and purple planar volumes) in drill holes BH1 and BH2. Modelling completed in Leapfrog using bounding deformation features, such as shear fractures (plotted in included stereonet). Zones I to IV are representative of the deformation zones present in one or both the drill holes, descriptions include in the text. N-S and E-W cross sections included on the right of the figure, with the N-S sections taken through each drill hole. B) 3D models at different scales to (a), with both quartz-calcite (D_5) and epidote-prehnite (D_1) modelled from drill core structures (included in associated stereonet plots).

III) A NE-SW striking shallowly S-dipping zone in both BH1 (92.03 m-96.33 m) and BH2 (83.33 m-84.51 m), characterised by a D_1 epidote cataclasite reworked by chlorite and zeolite deformation features (host rock fragments are overprinted by zeolite). These cataclasites are also cross-cut by D_4 zeolite-calcite and late D_5 quartz-calcite veins (dense vein network).

IV) More clearly intersected in BH2 (108.08 m-111.1 m), a moderately to shallowly SW-dipping zone characterised by intensely sheared D_2 sericite-chlorite gouge and phyllitic bands, with a broader damage zone of sericite and chlorite fractures, is also intersected at the base of BH1 (96.57 m-99.24 m).

The modelled zones crosscut each other, assumed here with no offsets or lateral terminations. Their true thicknesses range from 1 m to 6 m and exhibit some dip and thickness variation (as shown in N-S and E-W sections in Figure 8a). The zones display different orientation trends: with the D_2-related zones moderately S to SE-dipping, and D_3-related zones shallowly W-dipping.

To explore Smøla's deformation features across scales, 3D models were created for selected intervals, such as: D_5 quartz-calcite veins in BH2 (~10 m scale) or epidote-prehnite (D_1) veins in BH1 (~1 m scale) (Figure 8b). These models, along with Figure 8a (~100 m scale), demonstrate the systematic to semi-systematic fracture arrays at various scales. Additionally, they illustrate differences in aperture widths and potential strike extents among structures associated with different deformation episodes: D_2 structures, for example, typically have the widest apertures and longest strike extents, while D_1 features exhibit the smallest apertures and the least lateral continuity on average but have the highest number of fractures per modelled volume.

4.3 K-Ar geochronology and X-ray diffraction

Seven fault gouge samples (Table 2, Figure 9) were collected from drill holes BH2 (SK2008, SK2012, SK2015), BH4 (120714) (Figure 4), and outcrops on Smøla Island (SK1024_1, SK1029_1, SK1033_1) for dating of potential authigenic and synkinematic potassium (K)-bearing clays. The dated samples compositions by X-ray diffraction (XRD) is shown in Figure 10, with the K-Ar dating results in Table 3 and Figure 11a are sub-divided by grain size fraction for each sample (<0.1 to 6-10 µm). The orientations of the sampled structures (Figure 11b) is provided in the text as dip inclination (0-90°) and dip direction (0-360°). None of the samples have associated kinematics, apart from sample SK1033_1. The samples descriptions are ordered by interpreted deformation episode, with the full sample characterisations available in the supplementary material.

4.3.1 Field relationships and XRD results

Sample SK2012 is from a 25 cm-wide foliated gouge/phyllite to cataclasite interval (Figure 9a), oriented 15/320, in monzogranite. The zone has strong chlorite and sericite (D_2) mineralisation and host rock fragments. XRD results indicate the K-Ar ages are provided by K-bearing illite/muscovite and smectite. Both illite/muscovite and smectite content increases with

decreasing grain size fraction, with highest abundance in the <0.1 µm fraction. Quartz is present in the coarser size fractions (0.4-2 to 6-10 µm), deriving from groundmass or host rock fragments.

Sample SK2015 is from a 20 cm-wide well-milled, foliated, clay-rich gouge zone (Figure 9b), oriented 37/183. The interval is within a well-defined damage zone of highly fractured monzogranite. The gouge has abundant host rock and quartz-calcite vein fragments. XRD results show the K-Ar ages derived from illite/muscovite, smectite, and potassium feldspar. The illite/muscovite content increases in the finer fractions. The coarser fractions (2-6 to 6-10 µm) are quartz-dominated, with minor calcite and potassium feldspar.

Table 2. Summary of K-Ar samples collected from either drill holes BH2 and BH4, or field stations on Smøla Island.

Sample	Site/BH	Host rock	Orientation (dip/dip direction)	Deformation episode	Description
SK2012	BH2	Monzogranite, fault rock	15/320	D_2	From 108.3 m in BH2, involving a sheared and foliated gouge band, possibly phyllitic.
SK2015	BH2	Monzogranite, fault gouge	37/183	D_2	From 109.74 m in BH2, from a well-milled gouge, some residual veins, and lithic fragments present (possibly from host monzogranite).
SK1029_1	1029	Monzodiorite, fault gouge	80/166	D_2, D_3	Gouge sample, green, chloritic, structure sub-parallel/inclined to major E-W structure.
SK2008	BH2	Monzogranite, fault rock	10/285	D_3	From 79.7 m in BH2, involving a hydraulic breccia to crackle breccia with hematite-bearing veins.
SK1033_1	1033	Gabbro	80/155?	D_3	Possible fault gouge within saprolite zone.
120714	BH4	Diorite, clays	54/059	D_3, D_4	Collected at 31.3 m in BH4, involving friable gouge in shear band, clay rich, with zeolite veins.
SK1024_1	1024	Diorite, fault gouge	73/179	D_2, D_3	Sample from upper portion of exposed sub-vertical structure; well-developed gouge.

Field sample SK1029_1 is from a ~5 cm-wide chlorite-clay-rich gouge zone, within monzodiorite (Figure 9f), oriented 80/166 and extending >10 m. The zone is proximal and inclined to a major E-W structure, mapped as a second-order L3 lineament (Figure 2). XRD results indicate the K-Ar ages are from smectite, illite/muscovite, and zeolite. The size fractions are dominated by chlorite-smectite mixed clay (tosudite). Illite/muscovite is absent in finest fraction, but present in the 0.1-0.4 to 6-10 µm fractions. Zeolite is abundant in the coarser fractions (2-6 to 6-10 µm).

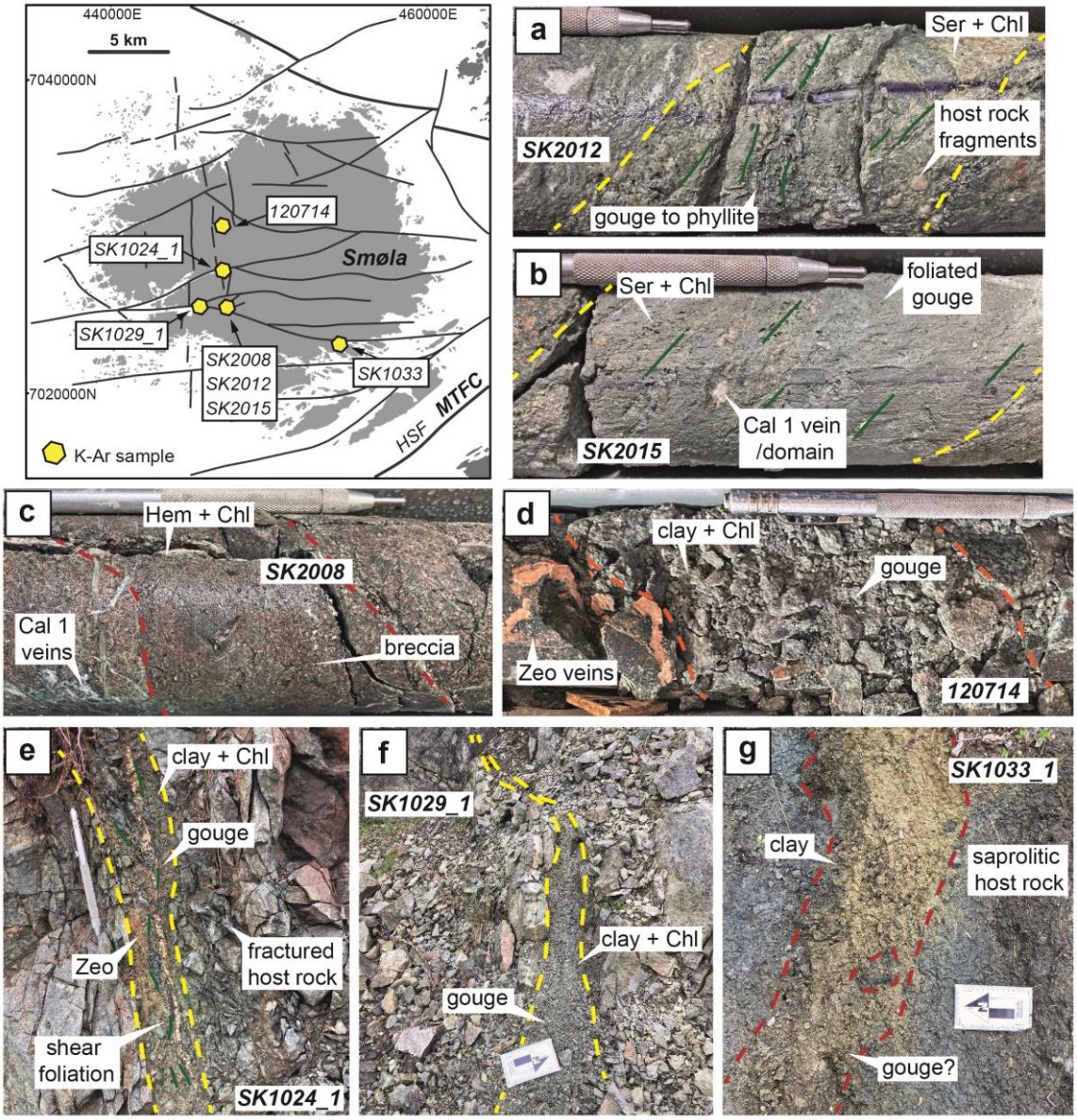

520 **Figure 9. The locations of the collected K-Ar samples on Smøla, relative to mapped lineaments. A-G) K-Ar sample sites, with samples SK2008, SK2012, and SK2015, 120714 collected from diamond drill core, and samples SK2024_1, SK1029_1, and SK1033_1 collected from field locations. Map adapted from DTM data courtesy of the NGU. Scratch pen for scale = 13 cm, or scale bar arrow = 10 cm.**

Sample SK2008 is from an 8 cm-wide indurated gouge to micro-vein breccia (Figure 9c), oriented 10/285. The interval is within a ~5 m wide damage zone of chlorite-hematite (D_3) mineralised and altered monzogranite. XRD results show the K-Ar
525 ages derived from illite/muscovite, smectite, and potassium feldspar. Hematite is present in all size fractions except the <0.1

μm fraction. Illite/muscovite is present in all fractions but a minor component in the <0.1 μm fraction. Smectite increases towards the finer fractions. The coarser fractions (2-6 to 6-10 μm) contain potassium feldspar, calcite, and quartz.

Field sample SK1033_1 is from a ~25 cm-wide possible weathered gouge zone within a saprolite horizon (Figure 9g), bound by adjacent chloritic-hematite slickensides, oriented 80/155 with low confidence (due to poor preservation), possibly dip-slip (slickenlines too subtle to orient accurately). XRD results indicate the K-Ar ages come from smectite and illite/muscovite. The size fractions are dominated by smectite, with minor chlorite, and illite/muscovite only present in coarsest fraction (6-10 μm).

Sample 120714 is from a 40 cm-wide friable clay-rich gouge within a shear band, oriented 54/059, in diorite, with cross-cutting zeolite veins (Figure 9d). XRD results show the K-Ar ages derived from smectite, illite/muscovite, and potassium feldspar. Smectite is dominant in all size fractions, comprising the <0.1 μm fraction entirely. Illite/muscovite is present in coarser fractions, and the 0.1-0.4 μm fraction. Potassium feldspar, plagioclase, and calcite are present in the coarser fractions (2-6 to 6-10 μm).

Field sample SK1024_1 is from a ~8 cm-wide foliated chloritic gouge zone (Figure 9g), oriented 73/179, within an 8 m wide damage zone with hematite fractures. The gouge zone, a D_2 to D_3 feature, is crosscut by zeolite veins. The XRD analysis for the finest fraction was not possible due to insufficient material. XRD results however indicate the K-Ar ages come from smectite, illite/muscovite, and zeolite. Minor illite/muscovite is present in all size fractions, with major amounts of smectite and chlorite. Zeolite and quartz are particularly abundant in the 0.4-2 to 6-10 μm size fractions.

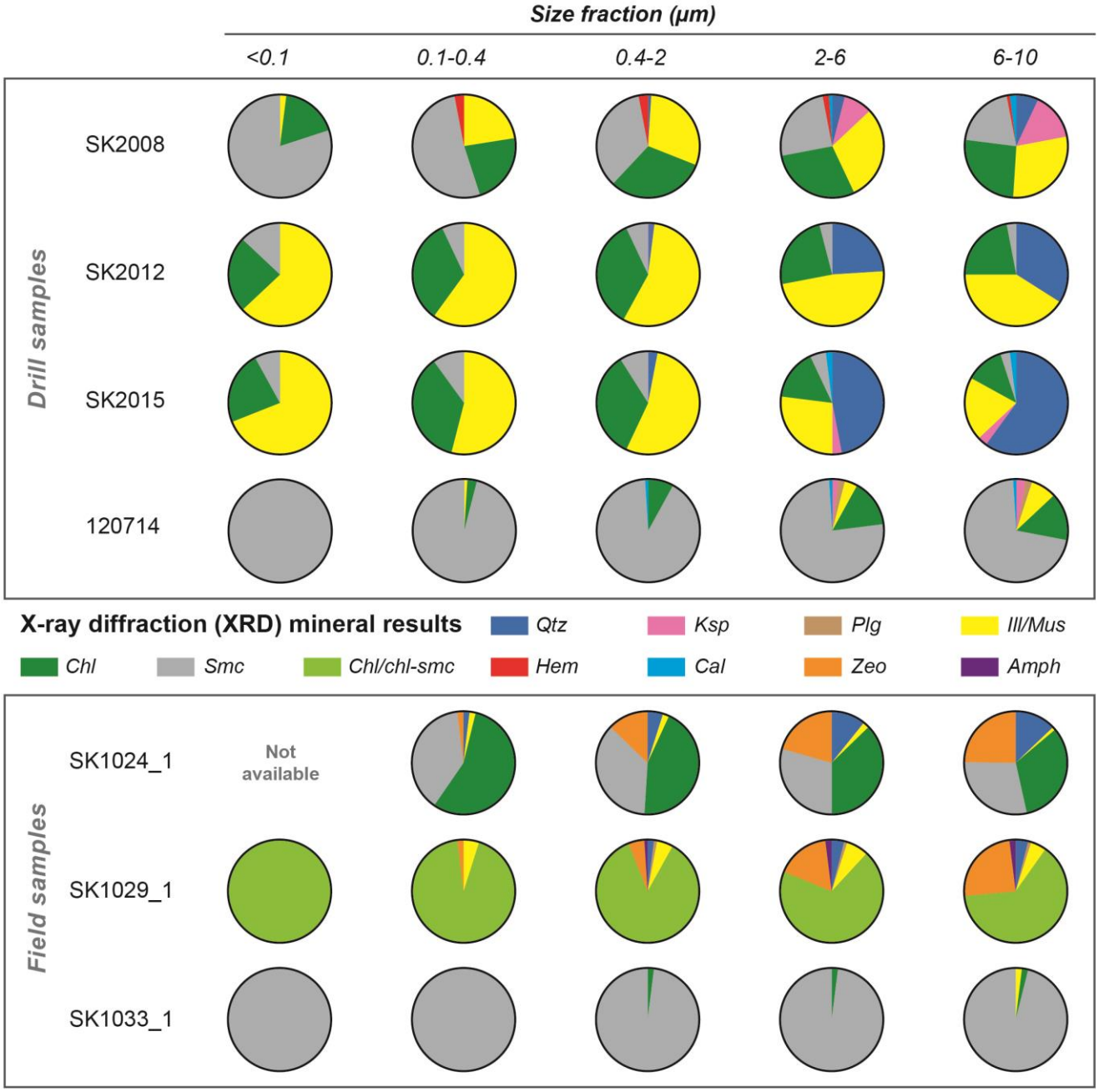

Figure 10. Pie charts with mineral compositions by weight percent (wt%) from X-ray diffraction results of the K-Ar samples. Mineral abbreviations: Qtz = quartz, Ksp = Potassic feldspar, Plg = plagioclase, Ill/mus = illite/muscovite, Chl = chlorite, Smc = smectite, Hem = hematite, Cal = calcite, Zeo = zeolite, Amp=amphibole. Note that due to poor crystallinity and/or the lack of structural data for mixed-layer clay minerals, only semi-quantitative assessments could be made.

4.3.2 K-Ar geochronology results

The K-Ar geochronology results (Figure 11 & Table 3) indicate that the samples can be grouped into four groups associated with mineral assemblages and deformation episodes (D_2 to D_4):

555

Associated with D_2, samples SK2012, SK2015, and SK1029_1 returned K-Ar ages for the finest fractions (<0.1 µm) of 196.1 ± 2.8 Ma, 201.4 ± 2.9 Ma, and 204.1 ± 3.7 Ma respectively. These ages likely correspond to authigenic illite-muscovite-smectite. Samples SK2012, SK2015 yielded coarsest fraction (6-10 µm) K-Ar ages of 290.7 ± 4.4 Ma and 287.0 ± 4.7 Ma respectively. Both samples SK2012, SK2015 have similar inclined age spectra curves with a plateau at ~300 Ma. The plateau
560 implies an inherited component (potentially inherited illite/muscovite) from an earlier tectonic episode. Sample SK1029_1 returned a much younger coarsest fraction K-Ar age of 218.2 ± 3.8 Ma. The younger ages are attributed to zeolite, with potentially radiogenic ^{40}Ar loss from the crystal structure, leading to lower age results (e.g. Levy and Woldegabriel, 1995).

Associated with D_3, samples SK2008, SK1033_1 yielded <0.1 µm fraction K-Ar ages of 99.6 ± 1.8 Ma and 128.1 ± 11.8 Ma
565 respectively, associated with likely authigenic illite-muscovite-smectite. The coarsest fractions provided ages of 195.2 ± 3.1 Ma and 263.3 ± 5.4 Ma respectively. The SK2008 fractions 0.4-2 to 6-10 µm have ages clustering at ~200 Ma, coinciding with the finest fraction ages for samples SK2012, SK2015, and SK1029_1, implying D_2 inheritance. The SK1033_1 ages may reflect authigenic clay growth during saprolite formation or hydrothermal activity, suggesting this sample's results should be treated with caution.

570

Sample 120714, associated with D_3 and D_4, yielded a <0.1 µm fraction K-Ar age of 74.7 ± 1.7 Ma, and a 6-10 µm fraction age of 153.6 ± 2.7 Ma. The finest fraction age is likely authigenic, but the coarsest fraction age, owing to the presence of potassic feldspar and illite/muscovite may represent an inherited/protolithic age. The zeolite veins (not in the XRD results), crosscutting the sampled gouge, would have mineralised after the ~75 Ma age, indicating a possible upper limit on the timing of D_4.

575

Sample SK1024_1 lacked enough material for the <0.1 µm fraction and is for demonstrative purposes only. The K-Ar ages range from 162.1 ± 3.1 Ma (0.1-0.4 µm fraction) to 163.5 ± 3.0 Ma (6-10 µm fraction), with the oldest age (180.5 ± 3.4 Ma) associated with the 0.4-2 µm fraction. The age spectra curve on Figure 11a, a convex-upward shape, indicates the zeolite presence in the coarser fractions is also lowering ages, like sample SK1029_1.

580

585

Table 3. K-Ar analysis age results of the Smøla samples by size fraction.

Sample			40Ar*			K			Age Data	
	Fraction (µm)	Mass (mg)	mol/g	σ (%)	40Ar* %	Mass (mg)	wt %	σ (%)	Age (Ma)	σ (Ma)
SK2008	<0.1	2.088	2.894E-10	0.57	40.4	50.6	1.63	1.76	99.6	1.8
	0.1-0.4	2.036	3.821E-10	0.54	53.9	51.6	1.46	1.78	144.9	2.6
	0.4-2	2.096	6.728E-10	0.50	77.2	52.8	1.79	1.74	204.7	3.5
	2-6	3.604	1.161E-09	0.46	89.6	52.2	3.06	1.64	206.5	3.3
	6-10	2.672	1.376E-09	0.47	94.7	51.0	3.85	1.58	195.2	3.1
SK2012	<0.1	2.016	2.065E-09	0.49	90.3	51.0	5.75	1.43	196.1	2.8
	0.1-0.4	3.654	2.221E-09	0.46	92.4	52.0	5.46	1.44	220.5	3.1
	0.4-2	2.938	2.716E-09	0.46	95.6	52.8	5.40	1.44	268.9	3.8
	2-6	2.524	2.536E-09	0.47	98.3	50.9	4.50	1.53	298.8	4.4
	6-10	2.452	2.106E-09	0.47	98.6	50.9	3.85	1.58	290.7	4.4
SK2015	<0.1	2.596	2.036E-09	0.47	90.4	51.5	5.51	1.44	201.4	2.9
	0.1-0.4	3.048	2.202E-09	0.46	93.1	51.3	5.33	1.46	223.7	3.2
	0.4-2	3.122	2.522E-09	0.46	95.5	51.6	5.16	1.47	261.8	3.8
	2-6	3.612	1.832E-09	0.46	97.0	51.1	3.37	1.62	289.1	4.5
	6-10	2.466	1.370E-09	0.47	98.4	50.9	2.54	1.69	287.0	4.7
120714	<0.1	2.750	5.869E-11	1.24	8.2	50.7	0.44	1.91	74.7	1.7
	0.1-0.4	1.368	1.122E-10	1.26	14.5	50.7	0.58	1.90	109.0	2.4
	0.4-2	3.600	1.844E-10	0.47	28.8	50.8	0.77	1.88	132.6	2.5
	2-6	2.710	2.786E-10	0.45	51.6	50.1	1.11	1.85	138.8	2.5
	6-10	2.554	3.933E-10	0.42	51.0	52.6	1.41	1.82	153.6	2.7
SK1024_1	0.1-0.4	2.220	1.982E-10	0.58	42.3	50.5	0.67	1.92	162.1	3.1
	0.4-2	1.600	3.118E-10	0.59	31.1	50.4	0.95	1.89	180.5	3.4
	2-6	2.568	3.196E-10	0.45	42.9	52.6	1.00	1.88	176.1	3.2
	6-10	3.186	2.926E-10	0.42	53.2	54.6	0.99	1.88	163.5	3.0
SK1029_1	<0.1	2.618	5.023E-10	0.41	50.4	51.3	1.34	1.85	204.1	3.7
	0.1-0.4	3.728	5.895E-10	0.38	57.3	57.2	1.18	1.85	267.3	4.7
	0.4-2	3.136	9.189E-10	0.38	77.4	56.0	1.54	1.82	314.9	5.4
	2-6	2.582	8.275E-10	0.39	84.9	62.8	1.92	1.76	232.8	3.9
	6-10	1.636	8.246E-10	0.45	88.3	52.5	2.05	1.78	218.2	3.8
SK1033_1	<0.1	2.224	1.814E-11	9.36	0.8	51.7	0.08	1.97	128.1	11.8
	0.1-0.4	2.236	2.085E-11	7.31	0.9	51.4	0.09	1.97	126.0	9.2
	0.4-2	2.854	9.294E-11	1.33	5.0	53.2	0.21	1.96	234.5	5.2
	2-6	3.042	1.020E-10	0.91	9.0	60.3	0.22	1.95	247.2	5.0
	6-10	2.354	1.219E-10	0.98	8.6	54.5	0.25	1.95	263.3	5.4

Overall, the K-Ar age results by structure orientation (Figure 11b) indicate that the D_2-associated structures striking NE-SW,
590 E-W, ENE-WSW yielded authigenic Triassic-Jurassic (~196 – 204 Ma) ages, with possible inherited Carboniferous-Permian (~287 – 291 Ma) ages. The D_3-associated structures striking NNE-SSW, ENE-WSW yielded authigenic Cretaceous (100 –

128(?) Ma) ages, with inherited Triassic-Jurassic (~200 Ma) material. Lastly, structures striking NW-SE, crosscut by later D_4 zeolite veins, yielded Cretaceous (75 Ma) ages.

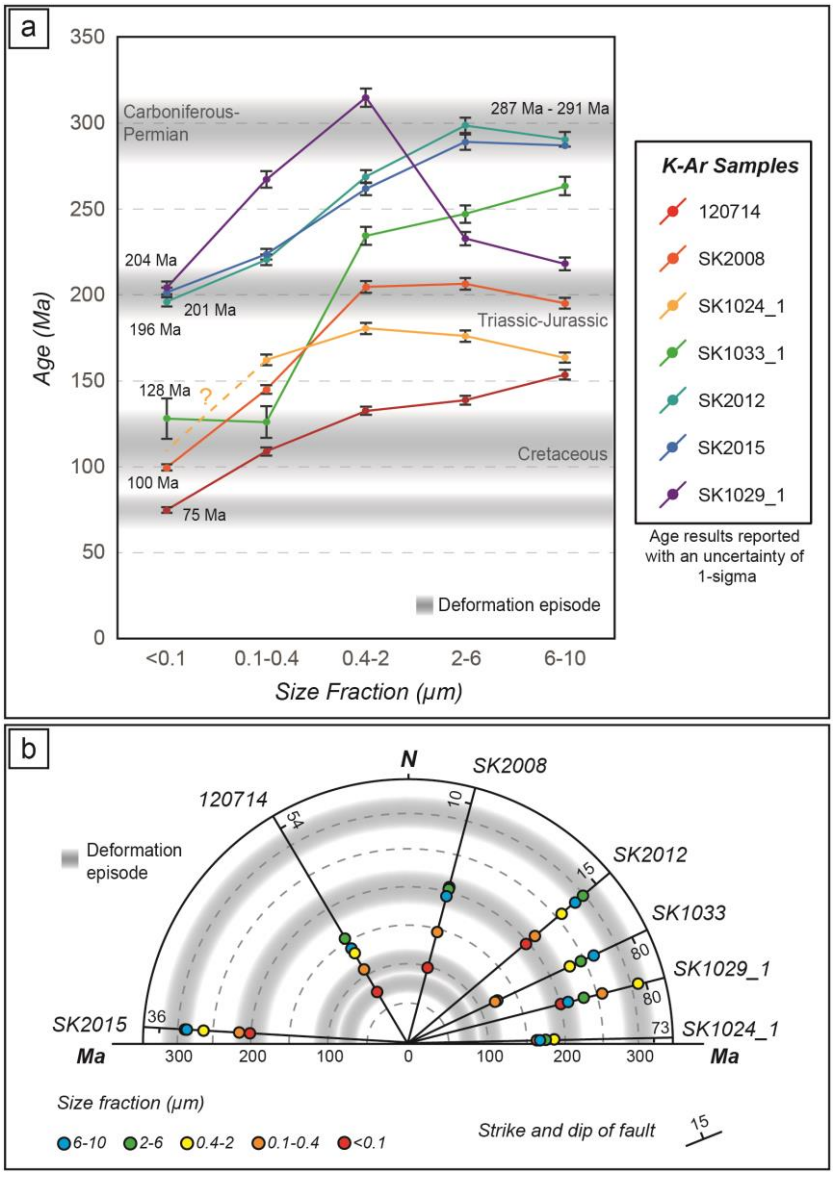

595

Figure 11. A) K-Ar age spectra results for the seven samples. Data are expressed by size fraction of the sampled medium against determined age, with age clustering indicating possible authigenic (and deformation) episodes; B) Radial plot showing dated samples with K-Ar ages and size fraction (coloured circles) plotted on lines indicating the strike orientations of sampled structures.

5 Discussion

5.1 Polyphase evolution of Smøla and the passive margin

Based on our new multiscalar and multi-technique results, we propose an evolutionary tectonic history for Smøla (Figure 12) and discuss its implications for the evolution of the passive margin:

The D_1 epidote-prehnite mineralisation, although not directly dated in this study, has been shown in other areas of the Norwegian margin to have formed from syn- to post Devonian times until ~290 Ma (Seranne, 1992; Sherlock et al., 2004; Indrevær et al., 2014; Watts et al., 2023). The D_1 brittle structures (Figure 5a, b, & Figure 8b) rework primary host rock features, and are systematically offset by the D_2 to D_5 structures, indicating that epidote and prehnite mineralised prior to all other deformation episodes (Figure 7). The D_1 tensile veins or sinistral strike-slip features, striking ENE-WSW (subvertical to steep SSE dips, shallow-plunging slip lineations) (Figure 3a), likely formed during post-Caledonian brittle sinistral transtension on the MTFC (Seranne, 1992; Watts et al., 2023) and WNW-ESE extension (represented on Figure 12).

Later, the NW-SE striking features (moderately to shallowly NE dipping), as well as the ~NNW-SSE to NNE-SSW striking features (steeply ~E dipping), being either normal dip-slip features or both dextral and sinistral (conjugate) features, may have formed because of local N-S to NNE-SSW shortening. This shortening direction is also implied by the Mid-Late Devonian development of E-W trending folds in the Edøyfjorden Basin Devonian rocks (Bøe et al., 1989 and Fossen, 2010) (Figure 12). From relative timing and structural data correlations, the lineaments L1, L2, L4, and L8, may have formed during D_1, with later reactivations. Overall, despite being the least strike-continuous features (as shown in the 3D model in Figure 8b), D_1 is pervasive across Smøla, the Devonian-aged Edøyfjorden Basin, and the WGR to the SE of the MTFC (Figure 2a & b.I, II).

The D_2 sericite-chlorite-calcite structures (Figure 5c, and Figure 6d & e) are dated to ~204-196 Ma (finest fractions for samples SK2012, SK2015, and SK1029_1 on Figure 11). However, microstructural and field evidence (Figure 6d & e) and the plateau in the age-spectra graph for the two coarsest fractions for SK2012 and SK2015 (Figure 11a), suggest a possibility of an earlier inherited deformation episode at ~300 Ma. Early faulting-related sericitisation of host rock feldspar (e.g. Wibberley, 1999) could explain the coarsest fraction illite/muscovite content and this inherited age. As such, two deformation (sub-)episodes may be associated with the sericite-chlorite-calcite mineral assemblage, and thus tentatively to D_2. Considering these two possible deformation phases, we can sort the complex array of D_2 structures (Figure 3a, b) into two structural frameworks: 1) The sinistral strike-slip ~E-W, and NE-SW striking features (moderately to steeply dipping ~N, SSW, NW), the normal faults striking ~N-S (moderately to steeply dipping W), and the ENE-WSW striking (steeply SSE dipping) reverse dip-slip features; and 2) the ENE-WSW striking (steeply SSE dipping) dextral strike-slip features, the ~N-S striking (steeply E dipping) reverse faults, and the ~E-W to NE-SW striking (moderately to steeply dipping ~N/S to SE) normal dip-slip features.

The first set of structures indicate sinistral strike-slip or transtension conditions along the MTFC, with ~WNW-ESE crustal extension and ~NNE-SSW shortening. This is largely consistent with the Late Carboniferous-Early Permian MTFC evolution as proposed by Seranne (1992) and Watts et al. (2023) (Figure 12). Furthermore, the ~N-S striking normal dip-slip features on Smøla have a similar geometry to the ~N-S extensional faults (Raudtinddalen Fault) off the VF, which have been associated with a similar age and kinematics (Watts et al., 2023). The moderately to shallowly south-dipping D_2 features in drill holes BH1 and BH2, as shown in 3D modelling (Figure 8a), likely coincide with the damage zone of the nearby major E-W structure. Adjacent to the drill holes, the major ~E-W structure also locally changes strike to a NW-SE trend (Figure 2b.I). The shallow dipping D_2 features, although possibly the result of local stress perturbations (e.g. Kim et al., 2004), may have formed from local shortening associated with the strike rotation of the major E-W structure (forming a restraining bend) (e.g. Cunningham and Mann, 2007) further supporting sinistral faulting.

Based on the above interpretation, the ~E-W, ENE-WSW, and NE-SW sinistral and reverse features may correspond to the L3, L4, and L5 (Figure 2b.I & II) second to third-order lineaments, and the ~N-S striking normal dip-slip features correlate with the L7 lineaments. Within this setting, the L5 lineaments could represent sinistral R and R' Riedel shears off the L3, L4 lineaments (Figure 2b.I), with the L7 lineaments predominantly involving extensional dip-slip features accommodating ~E-W/WNW-ESE extension. Additionally, during this phase, the L3 second-order lineaments which correlate with the major E-W structures and steep sinistral features (with sub-horizontal slip lineations) could also have formed as synthetic P-shears off the main MTFC trend (Figure 12). This earlier episode may therefore correspond to an overall NE-SW crustal stretching and rifting during the Late Carboniferous-Early Permian (timeline on Figure 12), resulting in the Late Palaeozoic basins such as the Froan Basin and Høybakken fault-related basin (Kendrick et al., 2004; Faleide et al., 2008; Peron-Pinvidic and Osmundsen, 2018).

The second set of structures may be associated with the ~200 Ma ages constrained by the finest grain size fractions of the D_2 associated samples. These structures suggest dextral strike-slip along the MTFC, with an overall extension direction ~NNE-SSW. Moreover, the steeply-dipping ENE-WSW striking dextral strike-slip features (with a horizontal slip lineation), being sub-parallel to the HSF (MTFC) trend, also correspond to the L4 lineaments. These L4 lineaments do show rare dextrally offsets of both the L1 and L2 lineaments, further suggesting some dextral kinematics is subtlety preserved (Figure 2b.I).

Based on the above interpretation, both the steep ~N-S striking reverse faults associated with D_2, and the major E-W structures (L3 lineaments) converging on the NE side of the Edøyfjorden Basin (Figure 2a) where there is a ENE-WSW to NE-SW strike rotation of the MTFC, may indicate a possible restraining band (associated with dextral strike-slip) (represented on Figure 12). As such, the E-W structures could represent a positive flower structure forming off the MTFC due to local transpression (e.g. Cunningham and Mann, 2007). The ~E-W to NE-SW moderately dipping normal features (with steeply plunging slip lineations) however indicate that over Smøla extensional conditions mostly prevailed, and many of the ~E-W structures formed

during earlier D_2 times, were reactivated as steep normal faults, or involve oblique dextral-normal kinematics. Additionally, the shallow D2 structures 3D modelled in Figure 8a, dipping south towards the major E-W structures might represent shallow-dipping antithetic or conjugate features formed during an extensional setting (related to late MTFC dextral faulting and extension). The shallow dipping D_2 structures in BH3 and BH4, in contrast, are within diorite and gneiss units (Figure 1b) and may involve the reactivation foliation planes during either early or late D_2 times, commonly associated with more micaceous intervals.

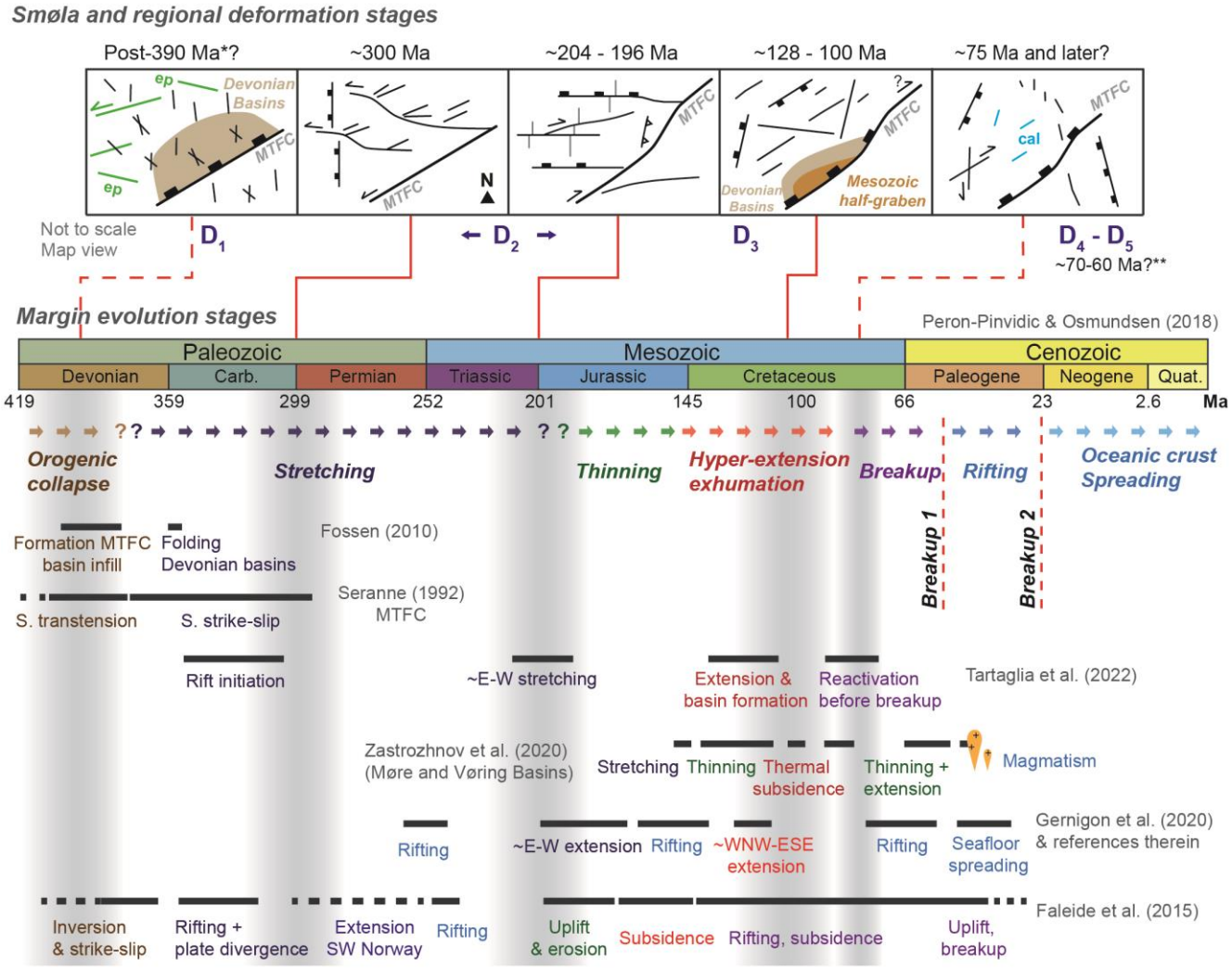

Figure 12. Summary figure integrating this study's results, represented at the top, relative to other Mid-Norwegian passive margin evolution studies. The main margin evolution stages are adapted from Peron-Pinvidic and Osmundsen, (2018). Ages provided by * Fossen et al. (2017), ** Hestnes et al. (2023).

Dextral kinematics on the MTFC (primarily on the VF) was proposed during the Jurassic by Grønlie and Roberts (1989), with Watts et al. (2023) however suggesting it occurred later along the VF, during the Late Jurassic/Early Cretaceous. The dextral strike-slip faulting could have resulted from poorly understood Triassic-Jurassic far-afield compressive forces acting on a mechanically weak MTFC and associated structures. However, at this time, the region was experiencing the start of an extensional phase with regional subsidence (Tsikalas et al., 2012; Peron-Pinvidic and Osmundsen, 2018), with commonly ~E-W crustal extension (Gernigon et al., 2020; Tartaglia et al., 2023) (shown on the timeline on Figure 12), which does not fit well with dextral kinematics, suggesting this tectonic phase remains uncertain.

Associated with D_3, the hematite-bearing structures (Table 2, Figure 9c, g) yielded finest size fraction K-Ar ages of between ~128 and ~100 Ma (Figure 11). Importantly, however, the ~128 Ma age from sample SK1033_1 may a reflect a saprolite age instead of D_3, even though most Norwegian margin saprolite ages correspond to Triassic/Jurassic ages (e.g. Fredin et al., 2017; Knies et al., 2022; Olesen et al., 2023). The age spectra plateau trend for sample SK2008, corresponding to ~200 Ma (fractions 0.4-2 to 6-10 µm), and the finest fraction K-Ar ages for samples SK2012, SK2015, and SK1029_1, also suggests a D_2 inheritance within the coarser fractions of this sample. Thus, the D_3 outcrops structures (Figure 3) can be sub-divided into two groups: 1) The majority of the normal to oblique-normal features striking NNE-SSW (dipping steeply W) and NE-SW (dipping moderately to steeply SE), the ~ENE-WSW sinistral strike to oblique-slip features (moderately to steeply NNE, SE dipping, with inclined to sub-horizontal slip lineations), and the ~NW-SE striking reverse dip-slip features (moderately ENE, and steeply SSW dipping); and 2) ~N-S striking (steeply W dipping) reverse faults, and the dextral features striking ENE-WSW (steeply NW dipping, inclined slip lineation, suggesting oblique-normal kinematics).

The first group of structures (dominated by dip-slip features, with steeply plunging slip lineations), being subparallel to the trace of the MTFC and the axis of the Edøyfjorden Basin, probably relate to a WNW-ESE to NW-SE extension, half-graben development, and Mesozoic sediment deposition within the Edøyfjorden Basin (Bøe and Bjerkli, 1989). A subset of pervasive L5, L7 lineaments (mostly third-order), also correspond to the moderately SE or steeply W-dipping normal dip- to oblique-slip faults, either formed or reactivated during D_3 (suggested by their lack of offset across the earlier lineaments). The strike-slip features however (mostly sinistral) could involve the coeval reactivation of steeply dipping D_2 sinistral features within an extensional setting. Associated to these features, some lineaments also have limited horizontal offsets of magnetic fabric over the D_3 lineaments (Figure 2b.II). Regionally, this relates to Jurassic-Cretaceous extension and exhumation, with regional rifting and basin development (Figure 12), leading to numerous Cretaceous basins (including the Møre and Vøring basins) (Faleide et al., 2008; Peron-Pinvidic and Osmundsen, 2018).

The second group of structures, particularly the steeply W-dipping ~N-S striking reverse faults, indicate ~E-W shortening. This corresponds to gentle folds (N-S oriented fold axes) in the Mesozoic basin rocks in the Edøyfjorden Basin (Bøe and Bjerkli, 1989). The steep NNW-SSE, N-S significant structures (red great circles on the D_3 'all planes' stereonets Figure 3)

and the shallowly SE/W dipping thrusts, which is 3D modelled on Figure 8a, are also associated to this setting. Geometrically, these folds indicate Late Mesozoic dextral transpressional conditions after dip-slip faulting on the HSF/MTFC, with ~E-W shortening of the basin sediments (Bøe and Bjerkli, 1989). Watts et al. (2023) however, associated the late dextral strike-slip kinematics with zeolite-calcite mineralisations on the VF (less distinct on the HSF; D_4 in this study).

The D_4 zeolite and calcite structures are not directly dated in this study (Table 2, Figure 9d, & Figure 11). However, these veins would have formed after ~75 Ma owing to cross-cutting relationships (Figure 9d). Tartaglia et al. (2023) and Watts et al. (2023) noted similar zeolite-calcite mineralisation in other parts of the margin (Hitra and Runde Islands) and on the Fosen Peninsula associated with the VF (only locally along the HSF). This mineralisation has been attributed to: I) earlier Mesozoic dextral strike-slip to transpressional faulting related to the N-S folds in the Edøyfjorden Basin (D_3 structures, this study); and II) later extensional dip-slip faulting on the HSF post-dating the zeolite-calcite features (Watts et al., 2023); or III) Late Cretaceous extension in the distal part of the rift margin (Gernigon et al., 2020; Tartaglia et al., 2023). The D_4 NNE-SSW and ENE-WSW sinistral/dextral faults, and associated L7 and L4 lineaments may therefore preserve evidence of the earlier D_3 Mesozoic (Jurassic) dextral strike-slip movement on the MTFC, and the NNE-SSW to NE-SW normal features (dipping ESE/W), with corresponding L2 and L8 lineaments, attributed to a later D_4 Cretaceous to Late Cretaceous (NW-SE) extension.

Representing the last Cretaceous-Palaeocene deformation episode, the D_5 quartz-calcite veins (Figure 5f, and Figure 6h & i) are similar to calcite veins U-Pb dated in W Norway and the WGR (Hestnes et al., 2023). Different veins oriented NE-SW yielded ages between ~90 Ma and ~80 Ma, associated with Cretaceous reactivation of the MTFC; ~NW-SE (and NE-SW) veins formed between ~70 Ma to 60 Ma, associated with regional uplift possibly related to the doming of the proto-Icelandic plume; and NE-SW veins forming <50 Ma, associated with different Cenozoic extensional processes (lithospheric flexure, uplift from far-field tectonic stresses) (Hestnes et al., 2023).

The D_5 structures, mostly normal dip-slip features or tensile veins, strike NE-SW (dipping steeply to moderately NW/SE), and NW-SE (steeply NE dipping) (Figure 3), and correspond to the L2, L5, L6, L7, and L8 lineaments. These structures and lineaments are mostly late reactivations of older features and are present in all parts of Smøla and SE of the MTFC (HSF) in the WGR (Figure 12). Overall, they suggest ~E-W to NE-SW crustal extension. Similar to these D_5 structures, and likewise indicating a late timing for D_5, Bøe and Bjerkli (1989) also documented NW-SE striking normal faults (SW/NE-dipping) offsetting Mesozoic sediments within the Edøyfjorden Basin. Based on geometry and timing, the D_4 and D_5 structures potentially relate to both a Cretaceous reactivation of the MTFC and the Cretaceous-Palaeocene rifting preceding the break-up of Greenland and Norway (Faleide et al., 2008). Importantly, the D_4 and D_5 features are subparallel to extensional structures offshore, particularly to the Klakk Fault Complex on the western side of the Frøya High, and the Halten Terrace, as well as the HD to the NW of Hitra and Frøya, suggesting a temporal and genetic association.

5.2 Smøla as an analogue for similar offshore basement volumes

Smøla Island represents an ideal onshore analogue for offshore basement highs in the area. The Frøya High, offshore Norway, as an example (owing to it having similar basement rocks as Smøla), is likewise bound by major structures, such as the Klakk Fault Complex, a major west-dipping extensional fault zone (Muñoz-Barrera et al., 2020). The Frøya High experienced a comparable polyphase deformation related to crustal stretching and thinning from the mid-Carboniferous to the Late Cretaceous-Palaeocene rifting (Faleide et al., 2008, 2015; Peron-Pinvidic and Osmundsen, 2018). To unravel its complex tectonic history, this structural high would therefore require a similar approach as our Smøla study. Although numerous drill holes have been completed along the mid-Norwegian margin, with at least three drill holes on Frøya (e.g. Slagstad et al., 2008; Bunkholt et al., 2022), the quality of the drill hole material is poor (only rock cuttings or rock plugs) (Muñoz-Barrera et al., 2020). Similarly, margin-wide geophysical (magnetic, gravity, and 2D, 3D seismic reflection surveys) datasets are also available (Skilbrei et al., 2002; Muñoz-Barrera et al., 2020), but most will only afford the ability to interpret at or above the seismic resolution-scale. The advantage, therefore, of using an onshore analogue such as Smøla is the access and the availability of numerous datasets, without these limitations.

Moreover, investigating fractured and weathered basement is crucial for understanding basement-hosted oil and gas reservoirs or fluid pathways (Trice, 2014; Trice et al., 2022). The petrophysical attributes of various deformation features associated with the D_1 to D_5 episodes could significantly impact fluid migration or storage. As these features exhibit cross-cutting relationships and different orientation trends, structural permeability anisotropy is clearly present in the Smøla basement volume. Therefore, using an onshore analogue to produce high-resolution structural characterisations aided by the absolute time dimension, may be crucial in the future understanding of basement-hosted plays offshore.

6 Conclusions

The integration of various methodologies and data types including multiscalar geophysical, drill core, outcrop, 3D modelling, microstructural data, and geochronological results, give the following key conclusions:

1) From regional to microscale evidence, we have identified five distinct tectonic episodes since the Devonian affecting Smøla associated with specific mineral assemblages and structural trends (Figure 12):
    I. The earliest D_1 episode is associated with epidote-prehnite syn- to post-Devonian ENE-WSW striking (subvertical to steep SSE dips) tensile veins and sinistral strike-slip features, from brittle sinistral transtension along the MTFC. A later ~N-S contraction resulted in NW-SE (moderate to shallow NE dips) normal features, and ~NNW-SSE to NNE-SSW (steep ~E dips) strike-slip features.
    II. The D_2 sericite-chlorite-calcite structures document two brittle-ductile phases, the first during the Carboniferous (~300 Ma), and a later during the Late Triassic-Early Jurassic (~204-196 Ma). The first phase accommodated sinistral strike-slip/transtension along the MTFC, associated with ~E-W and NE-SW sinistral strike-slip features

(moderate to steep ~N, SSW, NW dips), ~N-S normal faults (moderate to steep W dips), and ENE-WSW reverse faults (steep SSE dips). The second phase involved possible dextral strike slip along the MTFC (with local transpression related to a restraining bend east of the Edøyfjorden Basin), associated with ENE-WSW dextral strike-slip features (steep SSE dips), ~N-S reverse faults (steep E dips), and ~E-W to NE-SW normal features (moderate to steep ~N/S to SE dips).

III. The D_3 chloritic-hematite breccias and gouges are due to Cretaceous (~128-100 Ma) WNW-ESE to NW-SE extension and half-graben development and are coeval with Edøyfjorden Basin sediment infill. This episode is characterised by mostly dip-slip normal to oblique-normal features striking NNE-SSW (steep W dips), NE-SW (moderate to steep SE dips), the ~ENE-WSW oriented sinistral features (moderate to steep NNE, SE dips), and the ~NW-SE reverse faults (moderate to steep ENE, SSW dips). A possible later ~E-W shortening during dextral transpression on the MTFC also caused ~N-S trending folds within Mesozoic sediments (Edøyfjorden Basin) and ~N-S striking D_3 reverse faults (steep W dips).

IV. The D_4 hematite-zeolite-calcite structures form after ~75 Ma and are associated with NNE-SSW to NE-SW striking normal dip-slip faults and tensile veins (moderate to steep ESE/SE, W dips). These structures developed during Cretaceous to Late Cretaceous ~E-W crustal extension. Additionally, D_4 may have accommodated late Mesozoic dextral strike-slip movement on the MTFC, which is related to NNE-SSW and ENE-WSW striking sinistral/dextral features (moderate to steep ESE/NNW dips).

V. D_5, a possible Cretaceous to Paleogene episode, is associated with NE-SW (moderate to steep NW/SE dips), and NW-SE (steep NE dips) quartz-calcite shear (normal dip-slip) and tensile veins. These veins crosscut all previous deformation features. The D_5 features are likely to have formed during continued ~E-W/ NE-SW crustal extension related to reactivation of the MTFC and rifting preceding the Greenland-Norway break-up.

2) Using the drill logging results and the temporal constraints of this study, 3D modelling has revealed the complex geometric characteristics of basement deformation. The modelling allowed several deformation zones to be modelled, with four zones correlated between the BH1 and BH2, characterised by epidote veins (D_1), chlorite-sericite foliated gouge (D_2), chlorite-hematite breccia (D_3), and zeolite-calcite veins (D_4). For comparison, models were produced at scales of 100 m, 10 m, and 1 m based on D_2-D_4, D_5, and D_1 features. These models highlight how the D_2 structures possess the greatest size/strike extents, and the D_1 features the most localised. Additionally, the modelling provides indications that some of the zones (D_2, D_4) can be linked to adjacent major structures, such as inclined splays from the nearby major E-W structures.

This study presents a method for understanding the tectonic evolution and structural characterisation of basement volumes with complex geological histories. The approach used could be valuable for studying offshore structures, such as the Frøya High, and other fracture-hosted unconventional hydrocarbon reservoirs associated with basement highs.

Data availability

Relevant data analysed including lineament shapefiles, field, drill, structural, and XRD and K-Ar geochronology data are available at Mendeley Data, https://data.mendeley.com/datasets/2nmr2cz9yy/2 (last access 01 March 2024).

Supplement

The supplement related to this article is available online at Mendeley Data, https://data.mendeley.com/datasets/2nmr2cz9yy/2

Author contributions

MH undertook conceptualisation, data collection, sample collection, data curation, formal analysis, investigation, validation, writing-original draft and review and editing, and figure preparation. GVK did conceptualisation, data collection, sample collection, writing-final draft and review and editing. JK performed funding acquisition, conceptualisation, contribution-final draft, and review. RvdL undertook sample collection, K-Ar geochronology laboratory analyses, writing-final draft and review and editing. JS did XRD, and K-Ar geochronology laboratory analyses, writing-final draft and review and editing. ØN performed data collection, writing-final draft and review and editing. MB managed the drilling on Smøla Island. AN, undertook data collection, writing-final draft and review and editing. GV obtained funding, administrated the project in Bologna, performed early conceptualisation of the study, contributed to data and sample collection, acted as the PhD project supervisor, and contributed to the writing-final draft and review and editing.

Financial support

This research has been supported by the ongoing BASE 3 project ("BASE – Basement fracturing and weathering on - and offshore Norway"); and the Research Council of Norway (Norges Forskningsråd), grant no. 319849. BASE is a joint research project launched and steered by the Geological Survey of Norway (NGU), with the industry partners Equinor ASA, Lundin Norway AS, AkerBP ASA, Spirit Energy Norway AS, and Wintershall-Dea Norway AS, and the Norges Forskningsråd (NFR).

Acknowledgements

We thank all the BASE colleagues for the continuous discussion and constructive inputs. The NGU petrography laboratory is thanked for the assistance in the preparation of the thin sections. All the colleagues at the University of Bologna are specially thanked for their continual support and encouragement. Also, we would like to express a sincere appreciation and acknowledgement to the two reviewers for their constructive input during the review process.

References

Belaidi, A., Bonter, D.A., Slightam, C., and Trice, R.C., 2018, The Lancaster Field: Progress in opening the UK's fractured basement play: Petroleum Geology Conference Proceedings, v. 8, p. 385–398, doi:10.1144/PGC8.20.

Blenkinsop, T., Doyle, M., and Nugus, M., 2015, A unified approach to measuring structures in orientated drill core, *in* Geological Society Special Publication, Geological Society of London, v. 421, p. 99–108, doi:10.1144/SP421.1.

Bøe, R., Atakan, K., and Sturt, B.A., 1989, The style of deformation in on Hitra and Smøla. Central: Norges geologiske undersøkelse Bulletin, v. 414, p. 1–19.

Bøe, R., and Bjerkli, K., 1989, Mesozoic sedimentary rocks in Edøyfjorden and Beitstadfjorden, Central Norway: Implications for the structural history of the Møre-Trøndelag Fault Zone: Marine Geology, v. 87, p. 287–299, doi:https://doi.org/10.1016/0025-3227(89)90066-2.

Bruton, D.L., and Bockelie, J.F., 1979, The Ordovician Sedimentary Sequence on Smøla, West Central Norway: Norges geologiske undersøkelse Bulletin, v. 348, p. 21–31.

Bunkholt, H.S.S., Oftedal, B.T., Hansen, J.A., Løseth, H., and Kløvjan, O.S., 2022, Trøndelag Platform and Halten–Dønna Terraces Composite Tectono-Sedimentary Element, Norwegian Rifted Margin, Norwegian Sea: Geological Society, London, Memoirs, v. 57, doi:10.1144/m57-2017-13.

Corfu, F., Andersen, T.B., and Gasser, D., 2014, The Scandinavian Caledonides: Main features, conceptual advances and critical questions: Geological Society Special Publication, v. 390, p. 9–43, doi:10.1144/SP390.25.

Cunningham, W.D., and Mann, P., 2007, Tectonics of strike-slip restraining and releasing bends: Geological Society, London, Special Publications, v. 290, p. 1–12, doi:10.1144/SP290.1.

Davids, C., Wemmer, K., Zwingmann, H., Kohlmann, F., Jacobs, J., and Bergh, S.G., 2013, K-Ar illite and apatite fission track constraints on brittle faulting and the evolution of the northern Norwegian passive margin: Tectonophysics, v. 608, p. 196–211, doi:10.1016/j.tecto.2013.09.035.

Drake, H., Tullborg, E.L., and Page, L., 2009, Distinguished multiple events of fracture mineralisation related to far-field orogenic effects in Paleoproterozoic crystalline rocks, Simpevarp area, SE Sweden: Lithos, v. 110, p. 37–49, doi:10.1016/J.LITHOS.2008.12.003.

Faleide, J.I., Bjørlykke, K., and Gabrielsen, R.H., 2015, Geology of the Norwegian Continental Shelf, *in* Bjørlykke, K. ed., Petroleum Geoscience: From Sedimentary Environments to Rock Physics, Berlin, Heidelberg, Springer Berlin Heidelberg, p. 603–637, doi:10.1007/978-3-642-34132-8_25.

Faleide, J.I., Tsikalas, F., Breivik, A.J., Mjelde, R., Ritzmann, O., Engen, Ø., Wilson, J., and Eldholm, O., 2008, Structure and evolution of the continental margin off Norway and the Barents Sea: International Union of Geological Sciences, v. 31, p. 82–91, doi:10.18814/epiiugs/2008/v31i1/012.

Fediuk, F., and Siedlecki, S., 1977, Smøla. Description of the geological map (AMS-M 711) 1321 I - 1:50 000: Universitetsforlaget.

Fossen, H., 2010, Extensional tectonics in the North Atlantic Caledonides: A regional view: Geological Society Special Publication, v. 335, doi:10.1144/SP335.31.

Fossen, H., 1992, The role of extensional tectonics in the Caledonides of South Norway: Journal of Structural Geology, v. 14, p. 1033–1046.

Fossen, H., Khani, H.F., Faleide, J.I., Ksienzyk, A.K., and Dunlap, W.J., 2017, Post-Caledonian extension in the West Norway-northern North Sea region: The role of structural inheritance, *in* Geological Society Special Publication, Geological Society of London, v. 439, p. 465–486, doi:10.1144/SP439.6.

Fossen, H., Ksienzyk, A.K., Rotevatn, A., Bauck, M.S., and Wemmer, K., 2021, From widespread faulting to localised rifting: Evidence from K-Ar fault gouge dates from the Norwegian North Sea rift shoulder: Basin Research, v. 33, p. 1934–1953, doi:10.1111/bre.12541.

Fredin, O. et al., 2017, The inheritance of a Mesozoic landscape in western Scandinavia: Nature Communications, v. 8, doi:10.1038/ncomms14879.

Gautneb, H., 1988, Structure, age and formation of dykes on the island of Smøla, Central Norway: Norsk geologisk tidsskrift, v. 68, p. 275–288.

Gautneb, Ha., and Roberts, D., 1989, Geology and petrochemistry of the Smøla-Hitra batholith, Central Norway: Norges Geologiske Undersøkelse Bulletin, v. 416, p. 1–24.

Gee, D.G., Fossen, H., Henriksen, N., and Higgins, A.K., 2008, From the Early Paleozoic Platforms of Baltica and Laurentia to the Caledonide Orogen of Scandinavia and Greenland: International Union of Geological Sciences, v. 31, p. 44–51, doi:10.18814/epiiugs/2008/v31i1/007.

Geological Survey of Norway, 2021, Bedrock map of Norway 1:1 350 000.:

Gernigon, L., Franke, D., Geoffroy, L., Schiffer, C., Foulger, G.R., and Stoker, M., 2020, Crustal fragmentation, magmatism, and the diachronous opening of the Norwegian-Greenland Sea: Earth-Science Reviews, v. 206, doi:10.1016/j.earscirev.2019.04.011.

Gillespie, P.A., Holdsworth, R.E., Long, D., Williams, A., and Gutmanis, J.C., 2020, Introduction: geology of fractured reservoirs: Journal of the Geological Society, v. 178, p. jgs2020-197, doi:10.1144/jgs2020-197.

Grønlie, A., Naeser, C.W., Naeser, N.D., Mitchell, J.G., Sturt, B.A., and Ineson, P.R., 1994, Fission-track and K-Ar dating of tectonic activity in a transect across the Møre-Trøndelag Fault Zone, central Norway.: Norsk Geologisk Tidsskrift, v. 74, p. 24–34.

Grønlie, A., and Roberts, D., 1989, Resurgent strike-slip duplex development along the Hitra-Snåsa and Verran Faults, Møre-Trøndelag fault zone, Central Norway: Journal of Structural Geology, v. 11, p. 295–305, doi:10.1016/0191-8141(89)90069-2.

Hartz, E.H., B. Martinsen, B., Øverli, P.E., Lie, H., Ditcha, E.M., Schmid, D.W., and Medvedev, S., 2013, Newly Discovered Giant Oil Fields of North Sea - The Role of Fractured Basement Highs, *in* European Association of Geoscientists & Engineers, p. cp-365-00017, doi:10.3997/2214-4609.20131805.

Hestnes, Å., Drost, K., Sømme, T.O., Gasser, D., Scheiber, T., Linge, H., Chew, D., and Jacobs, J., 2023, Constraining the tectonic evolution of rifted continental margins by U-Pb calcite dating: Nature, Scientific Reports, doi:10.1038/s41598-023-34649-z.

Hestnes, Å., Gasser, D., Scheiber, T., Jacobs, J., van der Lelij, R., Schönenberger, J., and Ksienzyk, A.K., 2022, The brittle evolution of Western Norway – A space-time model based on fault mineralizations, K–Ar fault gouge dating and paleostress analysis: Journal of Structural Geology, v. 160, p. 104621, doi:10.1016/J.JSG.2022.104621.

Holcombe, R., 2013, Oriented Drillcore: Measurement, Conversion and QA/QC Procedures for Structural and Exploration Geologists: http://www.holcombe coughlinoliver.com/downloads/.

Holdsworth, R.E., McCaffrey, K.J.W., Dempsey, E., Roberts, N.M.W., Hardman, K., Morton, A., Feely, M., Hunt, J., Conway, A., and Robertson, A., 2019a, Natural fracture propping and earthquake-induced oil migration in fractured basement reservoirs: Geology, v. 47, p. 700–704, doi:10.1130/G46280.1.

Holdsworth, R.E., McCaffrey, K.J.W., Dempsey, E., Roberts, N.M.W., Hardman, K., Morton, A., Feely, M., Hunt, J., Conway, A., and Robertson, A., 2019b, Natural fracture propping and earthquake-induced oil migration in fractured basement reservoirs: Geology, v. 47, p. 700–704, doi:10.1130/G46280.1.

Indrevær, K., Stunitz, H., and Bergh, S.G., 2014, On Palaeozoic–Mesozoic brittle normal faults along the SW Barents Sea margin: Fault processes and implications for basement permeability and margin evolution: Journal of the Geological Society, v. 171, p. 831–846, doi:10.1144/jgs2014-018.

Kendrick, M.A., Eide, A., Roberts, D., and Osmundsen, P.T., 2004, The Middle to Late Devonian Høybakken detachment, central Norway: 40Ar–39Ar evidence for prolonged late/post-Scandian extension and uplift: Geological Magazine, v. 141, p. 329–344, doi:10.1017/S0016756803008811.

Kim, Y.S., Peacock, D.C.P., and Sanderson, D.J., 2004, Fault damage zones: Journal of Structural Geology, v. 26, p. 503–517, doi:10.1016/J.JSG.2003.08.002.

Knies, J. et al., 2022, Continental weathering and recovery from ocean nutrient stress during the Early Triassic Biotic Crisis: Communications Earth & Environment, v. 3, p. 161, doi:10.1038/s43247-022-00480-z.

Ksienzyk, A.K., Wemmer, K., Jacobs, J., Fossen, H., Schomberg, A.C., Süssenberger, A., Lünsdorf, N.K., and Bastesen, E., 2016, Post-Caledonian brittle deformation in the Bergen area, West Norway: results from K–Ar illite fault gouge dating: Norwegian Journal of Geology, v. 96, p. 275–299, doi:10.17850/njg96-3-06.

Mosar, J., Eide, E.A., Osmundsen, P.T., Sommaruga, A., and Torsvik, T.H., 2002, Greenland – Norway separation: A geodynamic model for the North Atlantic: Norwegian Journal of Geology, v. 82, p. 282–299.

Muñoz-Barrera, J.M., Rotevatn, A., Gawthorpe, R.L., Henstra, G.A., and Kristensen, T.B., 2020, The role of structural inheritance in the development of high-displacement crustal faults in the necking domain of rifted margins: The Klakk Fault Complex, Frøya High, offshore mid-Norway: Journal of Structural Geology, v. 140, doi:10.1016/j.jsg.2020.104163.

Nasuti, A., Olesen, O., Baranwal, O., and Dumais, M., 2015, Compilation of aeromagnetic data, *in* Olesen, O. et al. eds., Coop Phase 2 - Crustal Onshore-Offshore Project. NGU confidential Report , Norges geologiske undersøkelse, v. 063, p. 11–24.

Olesen, O., Rueslåtten, H.G., Schönenberger, J., Smelror, M., van der Lelij, R., Larsen, B.E., Olsen, L., Baranwal, V., Bjørlykke, A., and Brönner, M., 2023, Jurassic heritance of the geomorphology in Mid Norway: Norwegian Journal of Geology, v. 103.

Olsen, E., Gabrielsen, R.H., Braathen, A., and Redfield, T.F., 2007, Fault systems marginal to the Møre-Trøndelag Fault Complex, Osen-Vikna area, Central Norway: Norwegian Journal of Geology, v. 87, p. 59–73.

Osmundsen, P.T., Eide, E.A., Haabesland, N.E., Roberts, D., Andersen, T.B., Kendrick, M., Bingen, B., Braathen, A., and Redfield, T.F., 2006, Kinematics of the Høybakken detachment zone and the Møre–Trøndelag Fault Complex, central Norway: Journal of the Geological Society, v. 163, p. 303–318, doi:10.1144/0016-764904-129.

Passchier, C.W., and Trouw, R.A.J., 2005, Microtectonics: Berlin, Springer Science & Business Media.

Peron-Pinvidic, G., Manatschal, G., and Osmundsen, P.T., 2013, Structural comparison of archetypal Atlantic rifted margins: A review of observations and concepts: Marine and Petroleum Geology, v. 43, p. 21–47, doi:10.1016/J.MARPETGEO.2013.02.002.

Peron-Pinvidic, G., and Osmundsen, P.T., 2020, From orogeny to rifting: insights from the Norwegian 'reactivation phase': Scientific Reports, v. 10, doi:10.1038/s41598-020-71893-z.

Peron-Pinvidic, G., and Osmundsen, P.T., 2018, The Mid Norwegian - NE Greenland conjugate margins: Rifting evolution, margin segmentation, and breakup: Marine and Petroleum Geology, v. 98, p. 162–184, doi:10.1016/j.marpetgeo.2018.08.011.

Redfield, T.F., Torsvik, T.H., Andriessen, P.A.M., and Gabrielsen, R.H., 2004, Mesozoic and Cenozoic tectonics of the Møre Trøndelag Fault Complex, central Norway: constraints from new apatite fission track data: Physics and Chemistry of the Earth, Parts A/B/C, v. 29, p. 673–682, doi:https://doi.org/10.1016/j.pce.2004.03.005.

Riber, L., Dypvik, H., and Sørlie, R., 2015, Altered basement rocks on the Utsira High and its surroundings, Norwegian North Sea: Norwegian Journal of Geology, v. 95, p. 57–89.

Roberts, D., 1980, Petrochemistry and palaeogeographic setting of the Ordovician volcanic rocks of Smøla, central Norway: Norges geologiske undersøkelse Bulletin, v. 359, p. 43–60.

Roberts, D., and Gee, D.G., 1985, An introduction to the structure of the Scandinavian Caledonides., *in* The Caledonide orogen–Scandinavia and related areas, v. Part 1, p. 55–68.

Rønning, J.S., and Elvebakk, H., 2005, Onshore-Offshore Resistivity studies. Basement resistivity at the Frøya High.:

Scheiber, T., and Viola, G., 2018, Complex Bedrock Fracture Patterns: A Multipronged Approach to Resolve Their Evolution in Space and Time: Tectonics, v. 37, p. 1030–1062, doi:10.1002/2017TC004763.

Scheiber, T., Viola, G., van der Lelij, R., Margreth, A., and Schönenberger, J., 2019, Microstructurally-constrained versus bulk fault gouge K-Ar dating: Journal of Structural Geology, v. 127, doi:10.1016/j.jsg.2019.103868.

Scheiber, T., Viola, G., Wilkinson, C.M., Ganerød, M., Skår, Ø., and Gasser, D., 2016, Direct 40Ar/39Ar dating of Late Ordovician and Silurian brittle faulting in the southwestern Norwegian Caledonides: Terra Nova, v. 28, p. 374–382, doi:10.1111/ter.12230.

Seequent, T.B.S.C., 2022, Leapfrog Works: www.seequent.com/products-solutions/leapfrog-works.

Seranne, M., 1992, Late Paleozoic kinematics of the Møre-Trøndelag Fault Zone and adjacent areas, central Norway: Norsk geologisk tidsskrift, v. 72, p. 141–158.

Sherlock, S.C., Watts, L.M., Holdsworth, R.E., and Roberts, D., 2004, Dating fault reactivation by Ar/Ar laserprobe: an alternative view of apparently cogenetic mylonite–pseudotachylite assemblages: Journal of the Geological Society, v. 161, p. 335–338, doi:10.1144/0016-764903-160.

Skilbrei, J.R., Olesen, O., Osmundsen, P.T., Kihle, O., Aaro, S., and Fjellanger, E., 2002, A study of basement structures and onshore-offshore correlations in Central Norway: Norwegian Journal of Geology, v. 82, p. 263–279.

Slagstad, T., Davidsen, B., and Stephen Daly, J., 2011, Age and composition of crystalline basement rocks on the Norwegian continental margin: Offshore extension and continuity of the Caledonian-Appalachian orogenic belt: Journal of the Geological Society, v. 168, p. 1167–1185, doi:10.1144/0016-76492010-136.

Slagstad, T., and Kirkland, C.L., 2018, Timing of collision initiation and location of the Scandian orogenic suture in the Scandinavian Caledonides: Terra Nova, v. 30, p. 179–188, doi:10.1111/ter.12324.

Slagstad, T., Ramstad, R.K., Davidsen, B., and Barrére, C., 2008, Petrophysical and thermal properties of pre-Devonian basement rocks on the Norwegian continental margin: Geological Survey of Norway Bulletin, v. 448, p. 1–6.

Tanner, D.C., Buness, H., Igel, J., Günther, T., Gabriel, G., Skiba, P., Plenefisch, T., Gestermann, N., and Walter, T.R., 2020, Fault detection: Understanding Faults: Detecting, Dating, and Modelling, p. 81–146, doi:10.1016/B978-0-12-815985-9.00003-5.

Tartaglia, G., Ceccato, A., Scheiber, T., van der Lelij, R., Schönenberger, J., and Viola, G., 2023, Time-constrained multiphase brittle tectonic evolution of the onshore mid-Norwegian passive margin: GSA Bulletin, v. 135, p. 621–642, doi:10.1130/b36312.1.

Tartaglia, G., Viola, G., van der Lelij, R., Scheiber, T., Ceccato, A., and Schönenberger, J., 2020, "Brittle structural facies" analysis: A diagnostic method to unravel and date multiple slip events of long-lived faults: Earth and Planetary Science Letters, v. 545, doi:10.1016/j.epsl.2020.116420.

Terzaghi, R.D., 1965, Sources of Error in Joint Surveys: Géotechnique, v. 15, p. 287–304, doi:10.1680/geot.1965.15.3.287.

Trice, R., 2014, Basement exploration, West of Shetlands: Progress in opening a new play on the UKCS: Geological Society Special Publication, v. 397, p. 81–105, doi:10.1144/SP397.3.

Trice, R., Hiorth, C., and Holdsworth, R., 2022, Fractured basement play development on the UK and Norwegian rifted margins:

Tsikalas, F., Faleide, J.I., Eldholm, O., and Blaich, O.A., 2012, The NE Atlantic conjugate margins: Regional Geology and Tectonics: Phanerozoic Passive Margins, Cratonic Basins and Global Tectonic Maps, p. 140–201, doi:10.1016/B978-0-444-56357-6.00004-4.

Tucker, R.D., Robinson, P., Solli, A., Gee, D.G., Thorsnes, T., Krogh, T.E., Nordgulen, Ø., and Bickford, M.E., 2004, Thrusting and Extension in the Scandian Hinterland, Norway: New U-Pb Ages and Tectonostratigraphic Evidence: American Journal of Science, v. 304, p. 477–532.

Viola, G., Torgersen, E., Mazzarini, F., Musumeci, G., van der Lelij, R., Schönenberger, J., and Garofalo, P.S., 2018, New Constraints on the Evolution of the Inner Northern Apennines by K-Ar Dating of Late Miocene-Early Pliocene Compression on the Island of Elba, Italy: Tectonics, v. 37, p. 3229–3243, doi:https://doi.org/10.1029/2018TC005182.

Watts, L.M., 2001, The walls boundary fault zone and the Møre Trøndelag fault complex: a case study of two reactivated fault zones. [PhD thesis]: Durham University, 0–550 p.

Watts, L.M., Holdsworth, R.E., Roberts, D., Sleight, J.M., and Walker, R.J., 2023, Structural evolution of the reactivated Møre-Trøndelag Fault Complex, Fosen Peninsula, Norway: Journal of the Geological Society, doi:10.1144/jgs2022-139.

White, N.C., 2014, Geological Interpretation of Aeromagnetic Data (David J. Isles and Leigh R. Rankin): Economic Geology, v. 109, p. 1495–1496, doi:10.2113/econgeo.109.5.1495.

Wibberley, C., 1999, Are feldspar-to-mica reactions necessarily reaction-softening processes in fault zones? Journal of Structural Geology, v. 21, p. 1219–1227, doi:10.1016/S0191-8141(99)00019-X.

Zastrozhnov, D., Gernigon, L., Gogin, I., Planke, S., Abdelmalak, M.M., Polteau, S., Faleide, J.I., Manton, B., and Myklebust, R., 2020, Regional structure and polyphased Cretaceous-Paleocene rift and basin development of the mid-Norwegian volcanic passive margin: Marine and Petroleum Geology, v. 115, doi:10.1016/j.marpetgeo.2020.104269.